

# A geometric interpretation of eddy Reynolds stresses in barotropic ocean jets

Talía Tamarin\*

*Department of Earth and Planetary Sciences, Weizmann Institute of Science, Rehovot, Israel.*

James R. Maddison

*School of Mathematics and Maxwell Institute for Mathematical Sciences, University of  
Edinburgh, Edinburgh, United Kingdom*

Eyal Heifetz

*Department of Geophysical Atmospheric and Planetary Sciences, Tel Aviv University, Tel Aviv,  
Israel*

David P. Marshall

*Department of Physics, University of Oxford, Oxford, United Kingdom*

*\*Corresponding author address:* Department of Earth and Planetary Sciences, Weizmann Institute of Science, Rehovot 76100, Israel.

E-mail: talia.tamarin@weizmann.ac.il

## ABSTRACT

16 Barotropic eddy fluxes are analysed through a geometric decomposition of  
17 the eddy stress tensor. Specifically, the geometry of the eddy variance ellipse,  
18 a two-dimensional visualization of the stress tensor describing the mean eddy  
19 shape and tilt, is used to elucidate eddy propagation and eddy feedback on the  
20 mean flow. Linear shear and jet profiles are analysed and theoretical results are  
21 compared against fully nonlinear simulations. For flows with zero planetary  
22 vorticity gradient, analytic solutions for the eddy ellipse tilt and anisotropy  
23 are obtained that provide a direct relationship between the eddy tilt and the  
24 phase difference of a normal mode solution. This allows a straightforward  
25 interpretation of the eddy-mean flow interaction in terms of classical stability  
26 theory: the initially unstable jet gives rise to eddies which are tilted “against  
27 the shear” and extract energy from the mean flow; once the jet stabilises,  
28 eddies become tilted “with the shear” and return their energy to the mean  
29 flow. For a nonzero planetary vorticity gradient, ray-tracing theory is used to  
30 predict ellipse geometry and its impact on eddy propagation within a jet. An  
31 analytic solution for the eddy tilt is found for a Rossby wave on a constant  
32 background shear. The ray tracing results broadly agree with the eddy tilt  
33 diagnosed from a fully nonlinear simulation.

## 34 1. Introduction

35 The dynamics of large scale ocean motions are strongly dependent upon the effect of the small  
36 scale turbulent eddy field. The Gent-McWilliams parameterisation (Gent and McWilliams 1990;  
37 Gent et al. 1995) is now a key ingredient in coarse resolution ocean circulation models (e.g.,  
38 Fox Kemper et al. 2013) and can be interpreted as modelling the vertical flux of momentum due  
39 to eddy form stresses (Greatbatch 1998). This vertical transfer of momentum by eddies plays a  
40 fundamental role in the the dynamics of the large-scale circulation– for example it is a leading  
41 order term in the dynamics of the Souther Ocean (e.g., Johnson and Bryden 1989; Danabasoglu  
42 et al. 1994).

43 While horizontal eddy momentum fluxes are less significant from a global perspective, they can  
44 play important roles in the dynamics of inertial jets. For example, they influence the dynamics of  
45 western boundary currents, where they are instrumental in transferring energy between the mean  
46 flow shear and eddies (Waterman and Jayne 2011; Waterman et al. 2011; Waterman and Jayne  
47 2012). Horizontal eddy stress is not captured by the Gent and McWilliams parameterisation, and  
48 its effects are not typically represented in coarse resolution ocean models beyond the influence  
49 of increased explicit or numerical dissipation (see Eden 2010 for an exception). This paper fo-  
50 cuses on the study of the geometric properties of the local horizontal eddy momentum stress, and  
51 specifically studies these properties in a series of idealised barotropic shear and jet problems. The  
52 geometric framework holds promise for elucidating the important roles of the horizontal eddy mo-  
53 mentum fluxes in these systems, as well as for suggesting ingredients for a parameterization of  
54 their larger-scale effects.

55 In the mean barotropic vorticity equation, the eddies influence the mean flow through the di-  
56 vergence of an eddy vorticity flux *vector*. The vector flux, and hence the influence of the eddies

on the mean flow, is conveniently visualised in the usual manner via plots of directed arrows, with the length indicating the local magnitude of the flux and the orientation indicating the local direction. In the corresponding mean momentum equation, the eddies influence the mean flow through the divergence of an eddy momentum stress *tensor*, whose components are related to the eddy Reynolds stresses, and which is equal to the eddy velocity covariance tensor. This stress can no longer be visualised as directed arrows – instead the natural visualisation is as an oriented eddy variance ellipse (Preisendorfer 1988; Wilkin and Morrow 1994; Morrow et al. 1994), with a well-defined eddy ellipse tilt and eccentricity.

Eddy vorticity fluxes are equal to the divergence of an eddy momentum stress tensor, of which the velocity covariance (and hence the eddy Reynolds stresses) forms a part, through the Taylor-Bretherton identity (Taylor 1915; Bretherton 1966b; Plumb 1986). In the barotropic vorticity equation only the double divergence of the barotropic part of the momentum stress tensor can influence the mean dynamics directly. Specific geometric properties of the eddy velocity covariance which can influence the mean dynamics (i.e. which do not vanish under this double divergence) are identified in Waterman and Lilly (2015). Three dimensional quasi-geostrophic generalisations to the geometric eddy variance ellipse view are discussed in Hoskins et al. (1983), Marshall et al. (2012), and Maddison and Marshall (2013).

In the formulation we employ here, the average size of the eddy variance ellipse is proportional to the square root of the local eddy kinetic energy, and similarly to the square root of an average magnitude of the local eddy momentum stress<sup>1</sup>. The direction of the major axis indicates the direction in which the corresponding component of the eddy velocity leads to the largest variance

---

<sup>1</sup>In Wilkin and Morrow (1994) and Morrow et al. (1994), the semi-major axes of the ellipse scale with the principal velocity variances. In Waterman and Lilly (2015) the semi-major axes are set equal to the square root of the principal velocity variances. In this article, the semi-major axes are instead set equal to the square root of twice the principal velocity variances, in which case the ellipse yields a fit to observed values of eddy zonal velocity  $u'$  and eddy meridional velocity  $v'$ , on a  $u'-v'$  plot, as discussed in section 2 and shown in Fig. 10.

78 (Wilkin and Morrow 1994), and consequently the greatest stress. The ratio of the size of the el-  
79 lipse in the major and minor axis directions is equal to the square root of the ratio of the variances  
80 associated with the components of the eddy velocity in each of these directions, and similarly to  
81 the ratio of square root of the magnitude of the eddy stress due to these components. These prop-  
82 erties are illustrated in Fig. 1. The ellipse associated with the eddy velocity covariance tensor can  
83 be characterized by three key geometric properties: a magnitude, tilt, and eccentricity. Together  
84 these capture the complete structure of the local eddy momentum stress<sup>2</sup>. Formally these geo-  
85 metric properties arise from a principal component analysis of the eddy velocity covariance tensor  
86 (Preisendorfer 1988).

87 Eddy variance ellipses and their geometric properties are useful diagnostics to characterize the  
88 eddy field and its mean flow interactions. For example, eddy variance ellipses are used to compare  
89 observational and model eddy variability in Wilkin and Morrow (1994). Southern Ocean satel-  
90 lite altimetry derived eddy velocity covariance is analysed using this approach in Morrow et al.  
91 (1994). Associations between ellipse geometry and topography, and between anisotropy and the  
92 mean flow, are noted. A similar analysis is applied in Scott et al. (2008), and associations between  
93 the eddy velocity covariance and topography are not in general found, although some association  
94 between ellipse orientation and topographic features in the Southern Ocean is discussed. Zonal  
95 versus meridional velocity variance is analysed over regions of the Pacific Ocean in Huang et al.  
96 (2007) for observational data and a numerical ocean model. The magnitude of the ratio is depen-  
97 dent upon the time window over which the velocity field is averaged, prior to computing velocity  
98 variances via further averaging. A recent study in Stewart et al. (2015) extends these earlier studies

---

<sup>2</sup>A crucial point to note is that that the eddy variance ellipse does not relate directly to the spatial structure of the eddy field. A locally highly isotropic eddy variance ellipse does not imply that the eddies are physically circular – rather it implies that, at that location, there is no component of the eddy velocity which preferentially leads to local eddy stress.

99 using observational data and a  $1/12^\circ$  resolution ocean model. An association between increased  
100 velocity covariance anisotropy and topography is observed and, in the numerical model, an asso-  
101 ciation between topographical slope and near-bottom covariance orientation is found. Differences  
102 between near-surface and near-bottom eddy velocity covariance properties are studied via decom-  
103 position of the model velocities into barotropic and baroclinic components.

104 It is known from linear theory that perturbations lean with the shear in stable configurations,  
105 and against the shear in unstable configurations (e.g. Pedlosky 1987, section 7.3). Moreover in  
106 the idealised barotropic jet configuration of Waterman and Hoskins (2013) it is observed that eddy  
107 variance ellipses orient themselves in a manner consistent with stability properties of the mean  
108 flow. The time mean eddy variance ellipses show orientations consistent with instability in the  
109 upstream unstable region of the jet, and with wave radiation in the downstream region. Similar  
110 behaviour is observed in Klocker et al. (2016) in an idealised primitive equation model of the  
111 Antarctic Circumpolar Current.

112 The primary purpose of this paper is to provide an explicit link between predictions from linear  
113 stability theory and resulting eddy variance ellipses. The paper is organized as follows. Section 2  
114 reviews the local geometric properties of the eddy velocity covariance tensor: the kinetic energy,  
115 horizontal eddy momentum stress anisotropy, and horizontal eddy momentum stress tilt. These  
116 are related to eddy variance ellipse properties, and their relation to wave group propagation is  
117 discussed. In Section 3 these geometric properties are calculated for a piecewise linear shear  
118 layer and a piecewise linear jet on an  $f$ -plane. Analytic solutions are derived from linear theory,  
119 and in the latter case these solutions are compared against calculations from a fully non-linear  
120 numerical model. In a further numerical calculation the geometric properties are diagnosed for a  
121 piecewise linear jet on a  $\beta$ -plane, and the results are compared against the results for a zonally  
122 evolving barotropic jet described in Waterman and Hoskins (2013). In Section 4 ray tracing theory

123 is used to calculate eddy variance ellipse properties for the piecewise linear jet on a  $\beta$ -plane. The  
 124 predicted spatial patterns of the geometric properties are compared against those diagnosed from  
 125 the numerical model. The paper concludes in Section 5.

## 126 2. Eddy momentum stress decomposition

127 In this section the geometric decomposition of local horizontal eddy momentum stress are re-  
 128 viewed. For further details see, for example, Hoskins et al. (1983), Marshall et al. (2012), Water-  
 129 man and Hoskins (2013), and Waterman and Lilly (2015).

### 130 *a. Geometric decomposition and interpretation*

131 The mean barotropic vorticity equation is:

$$\frac{\partial \bar{q}}{\partial t} + \bar{\mathbf{u}} \cdot \nabla \bar{q} = -\nabla \cdot (\overline{\mathbf{u}'q'}), \quad (1)$$

132 where forcing and dissipation have been neglected,  $\nabla$  is the horizontal gradient operator, and  $t$   
 133 is time. A bar signifies a mean quantity and a prime denotes a deviation from the mean<sup>3</sup>. The  
 134 absolute vorticity is:

$$q = f + (\hat{\mathbf{z}} \times \nabla) \cdot \mathbf{u}, \quad (2)$$

135 where  $f$  is the planetary vorticity and  $\mathbf{u}$  is the non-divergent velocity with  $x$ - and  $y$ -components  $u$   
 136 and  $v$  respectively.

137 Via the Taylor-Bretherton identity (Taylor 1915; Bretherton 1966b; Plumb 1986) the eddy vor-  
 138 ticity flux  $\overline{\mathbf{u}'q'}$  can be related to the eddy velocity covariance tensor  $\overline{\mathbf{u}' \otimes \mathbf{u}'}$  via (Hoskins et al.

---

<sup>3</sup>The averaging operator is a Reynolds operator, commutes with the partial derivatives  $\partial/\partial x$ ,  $\partial/\partial y$ ,  $\partial/\partial t$  and satisfies a Cauchy-Schwartz inequality such that  $\overline{a'b'}^2 \leq \overline{a'^2} \overline{b'^2}$ , with  $\overline{a'^2} \geq 0$ .

139 1983):

$$\begin{aligned}\overline{\mathbf{u}'q'} &= (\hat{\mathbf{z}} \times \nabla) \cdot \overline{\mathbf{u}' \otimes \mathbf{u}'} - \hat{\mathbf{z}} \times \nabla K \\ &= \nabla \cdot \mathbf{T},\end{aligned}\tag{3}$$

140 where the eddy momentum stress tensor  $\mathbf{T}$  has components:

$$\mathbf{T} = \begin{pmatrix} N & M \\ M & -N \end{pmatrix}.\tag{4}$$

141 Here  $K$  is the eddy kinetic energy:

$$K = \frac{1}{2} (\overline{v'^2} + \overline{u'^2}),\tag{5}$$

142 and  $M$  and  $N$  are the eddy Reynolds stresses:

$$M = \frac{1}{2} (\overline{v'^2} - \overline{u'^2}),\tag{6a}$$

$$N = \overline{u'v'}.\tag{6b}$$

143 The flux tensor  $\mathbf{T}$  may be decomposed (Hoskins et al. 1983; Marshall et al. 2012; Waterman and  
144 Hoskins 2013):

$$\mathbf{T} = \gamma K \begin{pmatrix} \sin 2\theta & -\cos 2\theta \\ -\cos 2\theta & -\sin 2\theta \end{pmatrix},\tag{7}$$

145 where three geometric parameters appear: the eddy kinetic energy  $K$ , an eddy momentum stress  
146 anisotropy  $\gamma$  which is bounded  $0 \leq \gamma \leq 1$ , and an eddy momentum stress tilt  $\theta$ . These geometric  
147 parameters may be computed directly from the Reynolds stresses  $M$  and  $N$  (see e.g. Marshall et al.  
148 2012, equations 17 and 21).

149 At a given spatial location, the eddy velocity forms some general trace in a  $u'$ - $v'$  plot. The  
150 geometric properties in (7) can be related to an elliptical fit to this trace, with components:

$$\begin{pmatrix} \tilde{u}'(\phi) \\ \tilde{v}'(\phi) \end{pmatrix} = \begin{pmatrix} \tilde{u}_0 \cos \phi \\ \tilde{v}_0 \sin(\phi + \varepsilon) \end{pmatrix}.\tag{8}$$



Here  $\phi$  parameterises the ellipse and  $\tilde{u}_0$ ,  $\tilde{v}_0$ , and  $\varepsilon$  determine the specific ellipse geometry. If the bar corresponds to a long time average, then the eddy stress and eddy kinetic energy resulting from the observed local eddy velocity  $\mathbf{u}'$  are identical to those resulting from an eddy velocity which, on a  $u'-v'$  plot, traces along this ellipse at a constant rate of change of  $\phi$ . This ellipse is illustrated in Fig. 2a, and its relation to the signs of the Reynolds stresses  $M$  and  $N$  is shown in Fig. 2b.

With this ellipse definition, the eddy kinetic energy  $K$  is equal to one quarter of the mean square of the semi-major and semi-minor axes, and the tilt  $\theta$  is the angle of the ellipse major axis to the  $x$ -axis. The ratio of the semi-minor axis  $B$  to semi-major axis  $A$ ,  $r = B/A$ , is related to the anisotropy parameter  $\gamma$  via (Hoskins et al. 1983; Marshall et al. 2012):

$$\gamma = \frac{1 - r^2}{1 + r^2}. \quad (9)$$

The ratio of the focus separation  $2F$  to the major axis  $2A$ , equal to the ellipse eccentricity  $e$ , is given by:

$$e = \frac{F}{A} = \sqrt{\frac{2\gamma}{1 + \gamma}}. \quad (10)$$

Additional properties of the eddy velocity covariance tensor have previously been discussed in the literature. In Huang et al. (2007) and Scott et al. (2008) a non-dimensional zonal-meridional anisotropy is defined<sup>4</sup>:

$$\alpha = \frac{\overline{u'u'} - \overline{v'v'}}{\overline{u'u'} + \overline{v'v'}}, \quad (11)$$

which is related to the geometric decomposition via:

$$\begin{aligned} \alpha &= -\frac{M}{K} \\ &= \gamma \cos 2\theta. \end{aligned} \quad (12)$$

---

<sup>4</sup>This non-dimensional anisotropy is denoted  $\alpha$  in Huang et al. (2007), and  $M$  in Scott et al. (2008).

166 In Waterman and Lilly (2015) and Stewart et al. (2015) a dimensional anisotropy is defined<sup>5</sup>, equal  
 167 to one half of the difference between the maximal and minimal eddy velocity variance:

$$L = \frac{1}{4} (A^2 - B^2) = \gamma K. \quad (13)$$

168 This is further related to the geometry of the ellipse via:

$$L = \frac{1}{4} F^2 \quad (14)$$

169 where  $F$  is one half of the ellipse focus separation.

### 170 *b. Spatial structure and mean flow forcing*

171 The mean momentum equation is:

$$\frac{\partial \bar{\mathbf{u}}}{\partial t} + \bar{\mathbf{u}} \cdot \nabla \bar{\mathbf{u}} + f \hat{\mathbf{z}} \times \bar{\mathbf{u}} = -\frac{1}{\rho_0} \nabla (\bar{p} + \rho_0 K) - \hat{\mathbf{z}} \times (\nabla \cdot \mathbf{T}), \quad (15)$$

172 where again forcing and dissipation have been neglected,  $p$  is the pressure, and  $\rho_0$  is a constant ref-  
 173 erence density. Consider a flow oriented in the  $x$ -direction (or, more generally, rotate coordinates  
 174 locally so that the flow is in the  $x$ -direction). Then substitution of the geometric decomposition (7)  
 175 results in a zonal eddy momentum forcing:

$$\begin{aligned} & [-\hat{\mathbf{z}} \times (\nabla \cdot \mathbf{T})] \cdot \hat{\mathbf{x}} = \frac{\partial M}{\partial x} - \frac{\partial N}{\partial y} \\ & = (\gamma \nabla K + K \nabla \gamma) \cdot \begin{pmatrix} \cos(2\theta - \pi) \\ \sin(2\theta - \pi) \end{pmatrix} \\ & + 2\gamma K \nabla \theta \cdot \begin{pmatrix} \cos(2\theta - \frac{\pi}{2}) \\ \sin(2\theta - \frac{\pi}{2}) \end{pmatrix}, \end{aligned} \quad (16)$$

---

<sup>5</sup>Denoted  $L$  in Waterman and Lilly (2015) and Stewart et al. (2015), and  $\hat{M}$  in Hoskins et al. (1983).

which relates the local mean momentum forcing by the eddies to the geometric parameters  $K$ ,  $\gamma$ , and  $\theta$ , and to their local gradients.

Now limiting consideration to the case where zonal averaging is applied, the zonal mean zonal velocity forcing by the eddies is:

$$\begin{aligned} \frac{\partial M}{\partial x} - \frac{\partial N}{\partial y} = -\frac{\partial N}{\partial y} = & \left( \gamma \frac{\partial K}{\partial y} + K \frac{\partial \gamma}{\partial y} \right) \sin(2\theta - \pi) \\ & + 2\gamma K \frac{\partial \theta}{\partial y} \cos(2\theta - \pi). \end{aligned} \quad (17)$$

For zonally periodic systems, such as the idealised systems considered in this article, this local mean momentum forcing by the eddies cannot be balanced by a mean pressure gradient, and corresponds directly to a local mean acceleration. Differing geometric parameter patterns which lead to an eastward momentum tendency are illustrated in Fig. 3, and patterns which lead to a westward momentum tendency are illustrated in Fig. 4.

In more general cases, only the non-divergent component of the eddy momentum tendency is associated with a local forcing (see e.g. Maddison et al. 2015). A more general approach is taken in Waterman and Lilly (2015), where instead spatial patterns of geometric parameters which lead to local forcing of the mean absolute vorticity are considered.

### *c. Wave group propagation*

The intrinsic group velocity of a slowly varying wave packet under the WKB approximation (Buhler 2009, section 2.1.6) is related to the ellipse tilt angle  $\theta$ . This provides a link between the geometric properties of the eddy velocity covariance and wave activity propagation, which will be used to develop an analysis based upon ray tracing in section 4. For further details see Hoskins et al. (1983) (and also Maddison and Marshall 2013; Waterman and Hoskins 2013).

Consider a plane wave with stream function perturbation:

$$\psi' = \Re \left( \hat{\psi} e^{i(kx + ly - \omega t)} \right), \quad (18)$$

where  $k$  is the zonal wavenumber,  $l$  the meridional wavenumber, and  $\omega$  the angular frequency, with  $\mathbf{u}' = \hat{\mathbf{z}} \times \nabla \psi'$ . It follows that this leads to an anisotropy  $\gamma = 1$  and a tilt:

$$\tan \theta = -\frac{k}{l}. \quad (19)$$

The intrinsic group velocity (group velocity minus mean velocity) is (Hoskins et al. (1983) equations 11–15, Maddison and Marshall (2013) equation 2.60, Waterman and Hoskins (2013) equation 4):

$$\begin{aligned} \mathbf{c}_{gR} &= \begin{pmatrix} \frac{\partial \omega}{\partial k} \\ \frac{\partial \omega}{\partial l} \end{pmatrix} - \mathbf{u} \\ &= \frac{1}{(k^2 + l^2)^2} \begin{pmatrix} (k^2 - l^2) \frac{\partial \bar{q}}{\partial y} - 2kl \frac{\partial \bar{q}}{\partial x} \\ (k^2 - l^2) \frac{\partial \bar{q}}{\partial x} + 2kl \frac{\partial \bar{q}}{\partial y} \end{pmatrix} \\ &= \frac{1}{\frac{1}{2} q' q'} \mathbf{T} \nabla \bar{q}, \end{aligned} \quad (20)$$

where here the mean potential vorticity gradient  $\nabla \bar{q}$  is treated as a column vector. Substitution of the geometric decomposition (7) leads to (see e.g. Hoskins et al. 1983, equation 16):

$$\mathbf{c}_{gR} = \gamma \frac{K}{\frac{1}{2} q' q'} |\nabla \bar{q}| \begin{pmatrix} \cos(2\theta - \theta_{\nabla \bar{q}} - \frac{\pi}{2}) \\ \sin(2\theta - \theta_{\nabla \bar{q}} - \frac{\pi}{2}) \end{pmatrix}, \quad (21)$$

(noting that  $\gamma = 1$  here) with:

$$\theta_{CgR} = 2\theta - \theta_{\nabla \bar{q}} - \frac{\pi}{2}, \quad (22)$$

where  $\theta_{\nabla \bar{q}}$  and  $\theta_{CgR}$  are the angles that the mean potential vorticity gradient and intrinsic group velocity make with the  $x$ -axis respectively.

### 3. Geometric decomposition for piecewise linear flows

The approach used here for framing the wave instability problem is the counter-propagating Rossby wave (CRW) perspective (following Rossby 1939; Bretherton 1966a), which is an insightful pedagogical framework for explaining the fundamentals of linearized shear flows instabilities (see also Hoskins et al. 1985 and Davies and Bishop 1994). Heifetz et al. (1999) performed a case-study on the CRW interaction in the simple barotropic Rayleigh model (Rayleigh 1880), as well as a modified version consisting of a jet-like flow featuring two strips of vorticity with opposite signs. The growing normal mode solutions for these configurations, obtained by Heifetz et al. (1999), are used in the current study to diagnose and interpret the eddy fields in the geometric decomposition framework.

#### *a. Piecewise linear shear layer on an $f$ -plane*

Consider the Rayleigh (1880) model background velocity profile, whose zonal mean zonal velocity (Fig. 6a) and vorticity are given by:

$$\bar{u}(y) = \begin{cases} +\Lambda b & y \geq b \\ +\Lambda y & -b \leq y \leq b \\ -\Lambda b & y \leq -b \end{cases}, \quad \bar{q}(y) = \begin{cases} 0 & y > b \\ -\Lambda & -b < y < b \\ 0 & y < -b \end{cases}. \quad (23)$$

Let the bar and prime now indicate zonal mean and perturbation respectively. A linear perturbation evolves via the linearised absolute vorticity equation:

$$\frac{\partial q'}{\partial t} + \bar{u} \frac{\partial q'}{\partial x} = -v' \frac{\partial \bar{q}}{\partial y}. \quad (24)$$

The PV gradient  $\partial \bar{q} / \partial y$  is concentrated in two  $\delta$ -functions at  $y = \pm b$ . Vorticity perturbations away from these locations can neither grow nor decay, and hence the vorticity perturbations with time dependent amplitude are concentrated in  $\delta$ -functions at  $y = \pm b$ . For a given wavenumber  $k$  the

227 corresponding total perturbation is written:

$$q'_k(x, y, t) = Q_k(t) \left[ e^{i\varepsilon_k^{+b}} \delta(y-b) + e^{i\varepsilon_k^{-b}} \delta(y+b) \right] e^{ikx}, \quad (25)$$

228 where  $\varepsilon_k^{\pm b}(t)$  are the phases of two waves at  $y = \pm b$ . In an unstable configuration the ratio of  
 229 the two wave amplitudes asymptotes to one as the waves grow (Heifetz et al. 1999), and hence  
 230 here their amplitudes are both set equal to  $Q_k(t)$ . The perturbation stream function is (following  
 231 Heifetz et al. 1999):

$$\psi'_k(x, y, t) = -\frac{Q_k(t)}{2k} \left[ e^{i\varepsilon_k^{+b}} e^{-k|y-b|} + e^{i\varepsilon_k^{-b}} e^{-k|y+b|} \right] e^{ikx}. \quad (26)$$

232 Noting that, subject to zonal averaging:

$$\overline{u'q'} = \frac{\partial M}{\partial y}, \quad \overline{v'q'} = -\frac{\partial N}{\partial y}, \quad (27)$$

233 it follows that in regions where  $q' = 0$  the Reynolds stresses  $M$  and  $N$  are independent of  $y$ , and  
 234 hence  $M$  and  $N$  take uniform values in each of the three regions  $y < -b$ ,  $-b < y < b$ , and  $y > b$ .  
 235 Specifically, outside of the shear layer,  $|y| > b$ , the velocity perturbations are:

$$u'_k = iv'_k = \frac{Q_k(t)}{2} \left[ e^{i\varepsilon_k^{+b}} e^{k(y-b)} + e^{i\varepsilon_k^{-b}} e^{k(y+b)} \right] e^{ikx} \quad (28a)$$

$$u'_k = -iv'_k = -\frac{Q_k(t)}{2} \left[ e^{i\varepsilon_k^{+b}} e^{-k(y-b)} + e^{i\varepsilon_k^{-b}} e^{-k(y+b)} \right] e^{ikx} \quad (28b)$$

236 for  $y < -b$  and  $y > b$ , respectively. Substituting these into equations (6) yields:

$$M = N = 0 \quad \text{for } y < -b \text{ and } y > b, \quad (29)$$

237 as required. However inside of the shear layer,  $|y| < b$ , the velocity perturbations are:

$$u'_k = +\frac{Q_k(t)}{2} \left[ e^{i\varepsilon_k^{+b}} e^{k(y-b)} - e^{i\varepsilon_k^{-b}} e^{-k(y+b)} \right] e^{ikx} \quad (30a)$$

$$v'_k = -\frac{Q_k(t)}{2} i \left[ e^{i\varepsilon_k^{+b}} e^{k(y-b)} + e^{i\varepsilon_k^{-b}} e^{-k(y+b)} \right] e^{ikx} \quad (30b)$$

238 leading to:

$$M = + \frac{Q_k(t)^2}{4} e^{-2kb} \cos \epsilon_k, \quad (31a)$$

$$N = - \frac{Q_k(t)^2}{4} e^{-2kb} \sin \epsilon_k, \quad (31b)$$

239 for  $-b < y < b$ , where  $\epsilon_k = \epsilon_k^{+b} - \epsilon_k^{-b}$  is the (time independent) phase difference between the two  
 240 waves. The linearised normal mode solution then yields an analytic expression for the geometric  
 241 parameters in the eddy stress tensor decomposition within the shear layer:

$$K = \frac{Q_k(t)^2}{4} e^{-2kb} \cosh(2ky), \quad (32a)$$

$$\gamma = \text{sech}(2ky), \quad (32b)$$

$$\theta = \frac{\epsilon_k}{2} \pm \frac{\pi}{2}, \quad (32c)$$

242 where the sign in (32c) is chosen so that  $-\pi/2 \leq \theta \leq \pi/2$ .

243 The Reynolds stresses vanish outside the shear layer and have constant values within, in the  
 244 latter case depending on the phase difference between the two interacting waves. As illustrated in  
 245 Fig. 5,  $|M|$  ( $|N|$ ) is maximized when the phase difference is zero ( $\pi$ ). Outside the shear layer, the  
 246 superposition of the velocities always tends to cancel out  $M$  and  $N$ , regardless of the phase differ-  
 247 ence between the waves. Inside the shear layer, the phase difference determines how the velocities  
 248 interfere, and hence the resulting values of  $M$  and  $N$ . However, these values (and hence the tilt and  
 249 anisotropy) remain constant within the shear layer. This result is generalized in Appendix A for a  
 250 continuous vorticity profile and shown to hold between any two vorticity waves.

251 The eddy kinetic energy  $K$ , anisotropy  $\gamma$ , and eddy ellipses, corresponding to the most unstable  
 252 mode, are shown in Fig. 6. The eddy ellipse tilt is constant within the shear layer. The eddy kinetic  
 253 energy and anisotropy both vary inside the shear layer, with a minimum in the kinetic energy  
 254 and maximum in the anisotropy at the centre. However their product, equal to the dimensional

anisotropy  $L = \gamma K$ , is constant. This corresponds, as per equation (14), to a constant eddy ellipse focus separation within the shear layer. Outside the shear layer the eddy “ellipses” are circular, with undefined tilt and with decreasing eddy kinetic energy as  $y \rightarrow \pm\infty$ .

$N$  is constant within the shear layer and vanishes outside. This indicates that there is no mean momentum tendency due to the eddies away from  $y = \pm b$ . At  $y = +b$ , moving across the boundary from inside to outside the shear layer, the eddy kinetic energy and anisotropy both decrease (discontinuously) with an eddy tilt  $-\pi/2 < \theta < 0$  on the non-zero shear side. This corresponds to cases A and C of Fig. 3, and hence to a westward momentum tendency. Conversely at  $y = -b$ , moving across the boundary from outside to inside the shear layer, the eddy kinetic energy and anisotropy both increase (discontinuously) with an eddy tilt  $-\pi/2 < \theta < 0$  on the non-zero shear side. This corresponds to cases A and C of Fig. 4, and hence to an eastward momentum tendency. In both cases the unstable linear perturbation implies a local mean momentum tendency which opposes and decelerates the flow. In this idealised case the implied deceleration is applied over  $\delta$ -functions at  $y = \pm b$ .

As discussed in Heifetz et al. (1999), unstable solutions are composed of two phased locked counter propagating Rossby waves at  $y = \pm b$ , with the waves mutually amplifying each other and with a phase difference  $0 < \varepsilon_k < \pi$ . Conversely, for stable solutions the waves mutually destroy each other, with a phase difference  $-\pi < \varepsilon_k < 0$ . From equation (32c), the eddy ellipse for an unstable perturbation leans *against* the shear, with  $-\pi/2 < \theta < 0$ , while the eddy ellipse for a stable perturbation leans *with* the shear, with  $0 < \theta < \pi/2$ . This behaviour is as discussed in Marshall et al. (2012).

Linear stability analysis gives that the most unstable mode has wavenumber  $k_{max}$  with  $2k_{max}b \approx 0.797$  and phase difference  $\varepsilon_{k_{max}} \approx 0.646\pi$  (values from Heifetz et al. 1999). This yields an eddy tilt within the shear layer of  $\theta \approx -0.177\pi$ . Note that this differs from the value  $-\pi/4$  which might



279 be expected based upon the argument that the eddies should lean maximally according to the local  
 280 shear. This maximal tilt of  $-\pi/4$  would corresponds to a phase difference of  $\varepsilon = \pi/2$ . Linear  
 281 perturbation growth requires phase locking between the perturbations at  $y = \pm b$ , and hence the  
 282 phase difference  $\varepsilon_k$  and wavenumber  $k$  are not independent for growing perturbations – the choice  
 283 of one implies a value for the other. As discussed in Heifetz et al. (1999), the phase difference  
 284 of the fastest growing mode arises as a compromise – in particular increasing  $\varepsilon_k$  beyond  $\varepsilon_{k_{max}}$   
 285 (leading to an increased eddy tilt) implies an increased value of  $k$ , a decrease in the amplitude of  
 286 each wave as seen by the other, and a net decrease in the perturbation growth rate. This behaviour  
 287 is a manifestation of the nonnormality of the system (Heifetz and Methven 2005).

### 288 *b. Piecewise linear jet on an $f$ -plane*

289 Following a similar procedure as for the piecewise linear shear layer, one can find the analytic  
 290 linear normal mode solutions for a piecewise linear jet, which consists of two constant and opposite  
 291 sign vorticity strips (e.g., Heifetz et al. 1999).

292 The background profile (Fig. 7a) is given by

$$\bar{u}(y) = \begin{cases} 0 & y \geq b \\ \Lambda(b-y) & 0 \leq y \leq b \\ \Lambda(b+y) & -b \leq y \leq 0 \\ 0 & y \leq -b \end{cases}, \quad (33)$$

$$\bar{q}(y) = \begin{cases} 0 & y > b \\ \Lambda & 0 < y < b \\ -\Lambda & -b < y < 0 \\ 0 & y < -b \end{cases}.$$

In this case a non-neutral linear perturbation consists of three waves at each of the interfaces  $y = 0, \pm b$ , and the vorticity perturbation for a given wavenumber  $k$  is written as

$$q'_k(x, y, t) = [Q_k^b(t)e^{i\varepsilon_k^b}\delta(y-b) + Q_k^0(t)e^{i\varepsilon_k^0}\delta(y) + Q_k^{-b}(t)e^{i\varepsilon_k^{-b}}\delta(y+b)]e^{ikx}. \quad (34)$$

For a symmetric normal mode solution, which corresponds to equal growth rate of all three waves, one finds  $Q_k(t) = Q_k^b(t) = Q_k^{-b}(t) = Q_k^0(t)/2$ ,  $\varepsilon_k^b = \varepsilon_k^{-b}$ , and the corresponding stream function perturbation is (Heifetz et al. 1999)

$$\psi'_k(x, y, t) = -\frac{Q_k(t)}{2k} \left[ e^{-k|y-b|} + 2e^{i\varepsilon_k}e^{-k|y|} + e^{-k|y+b|} \right] e^{ikx}, \quad (35)$$

where  $\varepsilon_k \equiv \varepsilon_k^0 - \varepsilon_k^b = \varepsilon_k^0 - \varepsilon_k^{-b}$  is a time-independent phase difference.

On each side of the jet, the Reynolds stresses are again independent of  $y$ , and the geometric properties of the eddy ellipse are given by

$$K = \frac{Q_k(t)^2}{2} e^{-kb} \left[ \frac{1}{2} e^{-kb} \cosh(2ky) + e^{-2ky} (\cos \varepsilon_k + e^{kb}) \right] \quad (36a)$$

$$\gamma = \frac{\sqrt{1 + \frac{1}{4}e^{-2kb} + e^{-kb} \cos \varepsilon_k}}{\frac{1}{2}e^{-kb} \cosh(2ky) + e^{-2ky} (\cos \varepsilon_k + e^{kb})}, \quad (36b)$$

$$\tan 2\theta = \mp \frac{\sin \varepsilon_k}{\cos \varepsilon_k + \frac{1}{2}e^{-kb}}; \quad (36c)$$

where the negative sign in (36c) corresponds to the northward side of the jet with negative shear ( $0 < y < b$ ) and the positive sign to the southward side of the jet with positive shear ( $-b < y < 0$ ).

0). The eddy ellipse tilt is no longer directly proportional to the normal mode phase difference due to the interaction with the third vorticity wave, which gives an additional  $\frac{1}{2}e^{-kb}$  term in the denominator of (36c).

To examine the validity of the analytic normal mode solution, we compare the calculated eddy ellipse tilt and anisotropy to those found from a fully nonlinear simulation (Fig. 7). Details regarding the numerical model are given in Appendix B. The non-differentiable piecewise-linear jet in (33) is approximated by a smooth “tanh” profile whose vorticity is given by

$$q_0 = \frac{\Lambda}{2} \left[ 2 \tanh\left(\frac{y}{d}\right) - \tanh\left(\frac{y+b}{d}\right) - \tanh\left(\frac{y-b}{d}\right) \right] \quad (37)$$

where  $\Lambda$  is the shear, the interfaces of the layers are located at  $y = 0, \pm b$  ( $b = 75$  km), and  $d$  is a parameter that measures the relative thickness of the transition regions at the interfaces. In the limit  $d \rightarrow 0$ , one recovers the piecewise linear profile. Here a small value of  $d = 0.05b$  is chosen. The zonal mean flow of the approximated piecewise linear jet at the initial moment, at  $t = 0$  days, is shown in Fig. 8a (black solid line).

A snapshot of the relative vorticity at early stages of the simulation, after  $t = 57$  days (Fig. 7b), shows that the vorticity perturbation is localized at the three interfaces  $y = 0, \pm b$ . The system picks up a mode  $n = 3$  solution, corresponding to a wavelength of  $\lambda \approx 290$  km (the  $x$  domain size is  $L_x = 872$  km) and a normalized wavenumber of  $2kb = 3.24$ . Due to the quantization requirement of our periodic domain, this is slightly larger than the marginally most unstable normal mode  $2k_{max}b = 2.452$  (given in Heifetz et al. 1999, for the case of a jet in an infinite domain). Our normal mode solution has a phase difference of  $\epsilon_k \cong 0.418\pi$  (substituting  $2kb = 3.24$  in equation (20) of Heifetz et al. 1999), which gives from (36c) an eddy ellipse tilt of  $\theta \cong 0.194\pi$  on the northward side of the jet and  $\theta \cong -0.194\pi$  on the southward side of the jet. Hence, the eddy ellipse is tilted *against* the shear in each side of the jet, consistent with an unstable normal mode

329 solution, fluxing momentum out of the jet core and into its flanks. Note that the tilt angle found  
 330 here is not far from the one found for the single shear layer in the previous section ( $\theta \cong -0.177\pi$ ).  
 331 In addition, it is similar to the value one finds for the most unstable normal mode solution of the jet  
 332 in an infinite domain case,  $\theta \cong -0.208\pi$ , achieved by substituting in (36c) the theoretical values  
 333 for the infinite domain case ( $2k_{max}b = 2.452$  and  $\varepsilon_k \cong 0.628\pi$ ).

334 Fig. 7c,d show the zonally averaged eddy ellipse tilt and anisotropy, respectively, from the nu-  
 335 merical simulation (dashed red line) and the analytic normal mode solution (blue line). The an-  
 336 alytic solution is calculated by interpolating the stream function expression (35) for the normal  
 337 mode solution onto a numerical grid and differentiating to find the velocity field. The results are in  
 338 good agreement, and show that the eddy tilt is constant in each side of the jet, positive (negative)  
 339 in the negative (positive) shear, with a jump towards  $\pm\pi/2$  at  $y = 0$ . The anisotropy structure in  
 340 each of the layers is similar to that for the single shear layer case, though here it maximizes closer  
 341 to the edges  $y = \pm b$  rather than in the middle of the layer. Both  $M$  and  $N$  are constant within the  
 342 layers, and hence only the perturbation kinetic energy  $K$  controls the meridional structure of the  
 343 anisotropy  $\gamma$  (which is inversely proportional to  $K$ ).

344 The constant tilts remain close to the theoretical value even at later stages of the simulation, when  
 345 the waves merge into vortices (not shown). At much later stages of the development, however, the  
 346 linear solution does not describe the dynamics adequately. In addition, once the mean vorticity  
 347 gradient becomes nonzero, the tilt is no longer constant. This is examined in more detail in the  
 348 next section in which a background planetary vorticity gradient is added. Since there are many  
 349 similarities between the results obtained on the  $f$ -plane and  $\beta$ -plane, a more detailed discussion is  
 350 deferred until the latter case.

### 351 *c. Piecewise linear jet on a $\beta$ -plane*

352 A more physically relevant case is when a background planetary vorticity gradient is included.  
353 The normal mode solution derived in the previous section is no longer valid in this case. However,  
354 the fastest growing mode and its growth rate are very similar to those found for the zero beta case.  
355 In order to describe the meridional dependence of the tilt, ray tracing will be applied in Section 4,  
356 but first a qualitative description of the evolution of the flow is given.

#### 357 1) TIME EVOLUTION AND GEOMETRIC DECOMPOSITION

358 Fig.8 shows the initial flow as well as selected times of the zonal mean velocity (Fig. 8a), mean  
359 potential vorticity (Fig. 8b) and mean potential vorticity gradient (Fig. 8c). The initial zonal mean  
360 velocity (Fig. 8a, black solid line shows  $t = 0$  days) is identical to that used in the zero beta case,  
361 i.e. the smooth approximation of the piecewise linear jet. It satisfies the necessary conditions  
362 for barotropic instability, since the absolute vorticity gradient changes sign within the domain  
363 (Fig. 8c, black solid line). By  $t = 135$  days  $\approx 7\tau$  (where  $\tau = \frac{1}{\Lambda e^{-kb} \sin \epsilon_k} \approx \frac{1}{6 \cdot 10^{-7}} \text{ sec} \approx 19$  days, the  
364 inverse growth rate of the fastest growing wavenumber from the simulation, calculated from the  
365 linear theory for the unbounded jet on the f-plane given in Heifetz et al. 1999), the mean flow has  
366 become significantly weaker (red solid line in Fig. 8a), due to the transfer of energy from the mean  
367 flow to the eddies. At this instant, the behaviour of the system changes:  $\partial \bar{q} / \partial y$  ceases to change  
368 sign within the domain (red solid line in Fig. 8c), so the jet can no longer support the existence of  
369 linearly unstable solutions. Later on, *jet sharpening* can be identified (dashed blue line in Fig. 8a,  
370  $t = 172$  days  $\approx 9\tau$  days).

371 Snapshots of the total potential vorticity are shown in Fig. 9. At early times, the system behaves  
372 linearly, and the potential vorticity at the interfaces is characterized by a wavy structure, with a  
373 mode  $n = 3$  corresponding to a wavenumber  $k = 3.7 \times 10^{-6} \text{ m}^{-1}$  or normalized wavenumber of

374  $2kb = 3.24$  (Fig. 9a,  $t = 57$  days  $\approx 3\tau$ ). At later times ( $t = 115$  days  $\approx 6\tau$ , Fig. 9b), the solution is  
 375 dominated by vortices, which appear to be oriented (in spatial structure) against the shear in each  
 376 layer. The orientation of the vortices changes shortly afterwards (Fig. 9c,  $t = 155$  days  $\approx 8\tau$ ), and  
 377 become tilted with the shear (in spatial structure). This is consistent with the jet sharpening that  
 378 was identified (dashed blue line in Fig. 8a), where the mean flow strengthens as a result of up-  
 379 gradient eddy momentum fluxes into the core of the jet. Eventually, ( $t = 270$  days  $\approx 14\tau$ , Fig. 9d),  
 380 the vortices break nonlinearly and the system equilibrates.

381 The transition in the behaviour of the eddy-mean flow interaction can be seen by calculating the  
 382 eddy variance ellipse at different locations and times of the simulation. Fig. 10 shows scatter plots  
 383 of  $u'$  and  $v'$  at the interfaces  $y = \pm b, 0$  for three different times, as well as their corresponding  
 384 ellipses. At  $t = 57$  days  $\approx 3\tau$  (left column), the anisotropy is close to one near the interfaces,  
 385 and the eddy ellipses are elongated. In addition, the tilts are consistent with the linear instability  
 386 picture, i.e. positive (negative) tilt on the negative (positive) shear on each side of the jet. By  
 387  $t = 115$  days  $\approx 6\tau$ , anisotropy at the flanks  $y = \pm b$  has become gradually smaller (hence the eddy  
 388 ellipses appear more round), though they are still characterized by a tilt that implies barotropic  
 389 instability. However, this changes at later times ( $t = 155$  days  $\approx 8\tau$ ), when the ellipses at  $y = \pm b$   
 390 are tilted oppositely, implying that the eddies are fluxing momentum up-gradient into the jet, with  
 391 back-scatter of eddy energy to the mean flow. Note that at  $y = 0$  (the center of the jet), we always  
 392 find a large  $\gamma$ , and  $\theta = \pi/2$  (in fact,  $\theta = \pi/2$  or  $0$  is required by symmetry). Equivalently,  $N \cong 0$   
 393 and  $M > 0$ , the latter implying that  $\overline{v'^2} \gg \overline{u'^2}$  so that the eddy variance ellipse is elongated in the  
 394 meridional direction.

395 Fig. 11 shows the temporal development and meridional dependence of the zonally averaged  
 396 eddy ellipse tilt and anisotropy, and of the Reynolds stresses  $M$  and  $N$ . Fig. 11a confirms that  
 397 during the initial development of the system, in the time interval  $t < 135$  days  $\approx 7\tau$ , the eddy tilt

shows the signature of instability with positive tilts on the northward side of the jet and negative tilts on the southward side of the jet. Gradually, the tilt (absolute value) on both sides of the jet approaches  $\pi/2$ , until at  $t = 135 \text{ days} \approx 7\tau$  all the eddies within the jet are characterized by  $\theta = \pi/2$ . The tilt then flips, consistent with the onset of stability and the momentum fluxes being directed up-gradient into the core of the jet. This holds until approximately  $t = 172 \text{ days} \approx 9\tau$ . After that, there is an indication for another flip in the tilt, implying that the eddies are strengthening again. However, after  $t = 210 \text{ days} \approx 11\tau$  the tilt is single signed within the jet, and its sign changes periodically. This is consistent with the sign of  $N$  oscillating periodically after  $t = 210 \text{ days} \approx 11\tau$  (Fig. 11c).

Fig. 11b shows the time evolution of the eddy anisotropy. During the initial time development there are three distinct regions where anisotropy is close to unity, at each of the interfaces  $y = \pm b, 0$ . During the transition period ( $t = 135 \text{ days} \approx 7\tau$ ), this picture changes drastically, with anisotropy being maximized in a broad meridional region around the jet center (the quasi-circular area of anisotropy close to unity around  $t = 135 \text{ days} \approx 7\tau$ ). After  $t = 187 \text{ days} \approx 10\tau$ , eddy anisotropy becomes significantly smaller. However, there is a secondary (though smaller) peak in anisotropy at the jet core, around  $t = 238 \text{ days} \approx 12.5\tau$ . This is consistent with a similar secondary maximum observed in  $M$  (Fig. 11d).

Looking immediately to the north of the jet in the early stage of the evolution (at around  $t = 57 \text{ days} \approx 3\tau$ ), near the jet core the tilt decreases with latitude with  $\pi/4 < \theta \leq \pi/2$ , corresponding to panel F of Fig. 4 and a deceleration of the mean flow. The anisotropy decreases with latitude while the eddy kinetic energy increases, with  $0 < \theta < \pi/2$ . Their combined effect is a decrease in the value of  $L$  with latitude and a net acceleration of the mean flow. Hence, there is a competing effect between the anisotropy, which acts to accelerate the jet core, and the tilt and eddy kinetic energy, which act to decelerate the jet core. The net combined effect is a deceleration of the zonal

mean flow near the jet core. Conversely, after the tilt angle flips, the tilt increases with  $y$ , while kinetic energy and anisotropy decrease with  $y$ . Hence, all three act to accelerate the flow (Fig.3 F,A and C, respectively).

## 2) INTRINSIC GROUP VELOCITY AND RELATION TO EDDY ELLIPSE TILT

The direction of the intrinsic group velocity from the simulation, estimated from the ratio  $N/M$  as per Equation (22), is plotted in Fig. 12.

During the unstable period ( $t < 135$  days  $\approx 7\tau$ ), the eddy ellipse tilt is consistent with an inward directed group velocity. Shortly after the initial time development, by  $t = 25$  days  $\approx 1.3\tau$ , the implied group velocity direction is almost independent of  $y$  and  $c_{gRy}$  (the meridional component of  $y$ ) is negative on the northward side of the jet, and positive on the southward side of the jet. Hence, momentum is fluxed out of the jet. The direction of the implied intrinsic group velocity at  $t = 25$  days  $\approx 1.3\tau$  is approximately  $\theta c_{gR} \approx \mp 0.65\pi$  on the northwards and southward sides of the jet, respectively. Shortly afterwards, however, the direction of the implied intrinsic group velocity is no longer independent of  $y$ ; instead it increases in the northward side and decreases in the southward side of the jet, with  $\theta c_{gR} \rightarrow 0$  at the jet core.

As the jet transitions to the stable regime, once the absolute vorticity gradient ceases to change sign (at  $t = 135$  days  $\approx 7\tau$ ) and the eddy ellipse is meridionally elongated ( $\theta = \pi/2$ ), all the rays become zonal ( $\theta c_{gR} = 0$ ). Immediately thereafter, we enter the stable regime, with outward radiating rays. The sign of the eddy tilt flips and correspondingly the meridional component of the implied group velocity changes to positive on the northward side and northward and southward sides of the jet. Going away from the jet core, the ray becomes refracted such that it becomes more meridional.



### 3) COMPARISON WITH WATERMAN AND HOSKINS (2013)

A comparison can be made between the results obtained here and those obtained by Waterman and Hoskins (2013) for the case of a zonally evolving jet in statistically steady state. In Waterman and Hoskins (2013) an unstable jet is forced at the boundary of the domain, and the geometric properties of the eddy velocity covariance tensor are defined via time mean averaging, rather than zonal averaging. The analysis shows a similar picture to that described here: eddies tilting against the shear in the upstream unstable region, and an eddy tilt consistent with wave radiation in the downstream stable region. The broad structure of  $M$ ,  $N$ ,  $K$  and the corresponding eddy ellipses described in Waterman and Hoskins (2013) are remarkably similar to those found here, though, importantly, in Waterman and Hoskins (2013) the structure varies spatially along the flow direction, whereas here the structure varies temporally through the flow evolution.

There are, however, some key differences. First, in Waterman and Hoskins (2013), the location where the eddy kinetic energy maximizes occurs downstream of the location where the potential vorticity gradient ceases to change sign as a consequence of mean flow advection, whereas here they occur simultaneously in time (at  $t = 135 \text{ days} \approx 7\tau$ ). At the point of maximum eddy kinetic energy Waterman and Hoskins find a “bullet of  $M$ ”, implying meridional elongation of the eddies there. Downstream of eddy kinetic energy maximum, Waterman and Hoskins find that forcing solely from  $M$  is responsible for strengthening and extending the jet, eventually forcing their time-mean recirculation gyres. A similar “bullet of  $M$ ” is found here (Fig. 11d) and meridional elongation at the time of maximum eddy kinetic energy. However, since a zonally symmetric jet is being considered here, the zonal mean vorticity forcing from  $M$  vanishes identically, and the mean flow forcing arises solely from  $N$ . Hence, no recirculation gyres can develop in our configuration, and the eddy forcing is instead responsible only for the acceleration or deceleration of the jet.

#### 467 **4. Ray tracing**

468 For a barotropic jet on a  $\beta$ -plane during the unstable regime, the eddy ellipse tilt is no longer  
469 constant within the shear layers (see Fig. 14a), but rather it increases towards the jet core. This  
470 effect is due to the nonzero potential vorticity gradient within the shear layers, and is intrinsically  
471 related to the wave propagation there.

472 Here ray tracing theory is employed to study the propagation of waves within the shear layers  
473 under the influence of the  $\beta$  effect and a constant shear. The analytic solution obtained from  
474 the ray equations agrees well with the fully nonlinear simulation, aiding in the prediction of the  
475 meridional structure of the eddy ellipse tilt.

##### 476 *a. Theoretical background*

477 The wave activity propagates at the group velocity. In a homogeneous medium a ray (which is  
478 the path parallel to the group velocity at every point) will propagate in a straight line. In an inho-  
479 mogeneous medium, however, refraction can occur. Ray tracing theory (Whitham 1974; Lighthill  
480 1977, also see Buhler 2009 and Salmon 1998 for overviews) gives the leading order asymptotic de-  
481 scription of a slowly varying wave packet in a medium that varies slowly compared to the scale of  
482 the waves (through the WKB approximation, see Hoskins and Karoly 1981; Hoskins and Ambrizzi  
483 1993).

484 For such conditions, the stream function can be represented locally by a plane wave,

$$\psi(x, y, t) \sim \hat{\psi} e^{i\phi(x, y, t)} \quad (38a)$$

$$\phi \approx kx + ly - \omega t, \quad (38b)$$

485 where

$$\omega(x, y, t) = -\frac{\partial \phi}{\partial t}, \quad k(x, y, t) = \frac{\partial \phi}{\partial x}, \quad l(x, y, t) = \frac{\partial \phi}{\partial y} \quad (39)$$

486 are slowly varying. Note that here a distinction is made between the local value of  
 487 the angular frequency,  $\omega(x, y, t)$ , and the dispersion relation,  $\Omega(k, l, x, y, t)$ , with  $\omega(x, y, t) =$   
 488  $\Omega(k(x, y, t), l(x, y, t), x, y, t)$ .

489 Cross-differentiation yields the ray equations

$$\frac{dk}{dt} = -\frac{\partial \Omega}{\partial x}, \quad \frac{dl}{dt} = -\frac{\partial \Omega}{\partial y}, \quad (40)$$

490 along rays defined by

$$\frac{dx}{dt} = c_{gx} = \frac{\partial \Omega}{\partial k}, \quad \frac{dy}{dt} = c_{gy} = \frac{\partial \Omega}{\partial l}, \quad (41)$$

491 where

$$\frac{d}{dt} = \frac{\partial}{\partial t} + \mathbf{c}_g \cdot \nabla. \quad (42)$$

492 These are equivalent to Hamilton's equations. In the absence of explicit time dependence in  
 493  $\Omega(k, l, x, y, t)$ , the analogue of the Hamiltonian, is conserved along ray path.

#### 494 *b. Analytic ray tracing solution*

495 In the case considered here, away from the interfaces, the solutions can be approximated as  
 496 plane wave whose dispersion relation is governed by the Rossby wave dynamics and given by

$$\Omega = \bar{u}k - \frac{\beta k}{k^2 + l^2}. \quad (43)$$

497 It follows that

$$\frac{dk}{dt} = 0, \quad \frac{dl}{dt} = -k \frac{\partial \bar{u}}{\partial y} = \pm k \Lambda; \quad (44)$$

$$\frac{dx}{dt} = \bar{u} + \frac{\beta(k^2 - l^2)}{(k^2 + l^2)^2}, \quad \frac{dy}{dt} = \frac{2\beta kl}{(k^2 + l^2)^2}, \quad (45)$$

where  $\pm$  refers to  $y > 0$  and  $y < 0$  respectively. Hence,

$$k = k_0, \quad l = l_0 \mp k_0 \Lambda t \quad (46)$$

where  $k_0$  and  $l_0$  are initial zonal and meridional wavenumbers.

The ray equations (44) and (45) may be solved analytically (see Appendix C for a full derivation). The analytic solution for the eddy ellipse tilt as a function of the meridional location gives

$$\theta(y) = \pm \frac{1}{2} \cos^{-1} \left( \cos 2\theta_0 \pm \frac{2\Lambda k_0^2}{\beta} (y - y_0) \right). \quad (47)$$

where  $\pm 2\Lambda k_0^2/\beta$  is positive in the northward side of the jet ( $y > 0$ ) and negative in the southward side of the jet ( $y < 0$ ). This expression allows the investigation of how the ray solution depends on the parameters of the problem, namely  $\beta$ ,  $k_0$  and the shear  $\Lambda$ . Note that the solution, conveniently, does not depend explicitly on  $l_0$ , but rather on the initial tilt  $\theta(y_0) = \theta_0$ , which can be calculated directly from the Reynolds stresses.

For example, for an outward radiating ray on the northward side of the jet, originating at the jet center, we would have  $y_0 = 0$ ,  $\theta_0 = \pi/2$  and  $\partial \bar{u}/\partial y = -\Lambda$ , giving

$$\theta(y) = \frac{1}{2} \cos^{-1} \left( \frac{2\Lambda k_0^2}{\beta} y - 1 \right), \quad (48)$$

which is only valid for  $0 < y \leq \beta/\Lambda k_0^2$ .

For nonzero  $\beta$  and  $\Lambda$ , going away from the jet core towards the flank at  $y = b$ , the tilt becomes gradually smaller, approaching  $\theta \rightarrow 0$  for  $y \rightarrow \beta/\Lambda k_0^2$ . This is consistent with the results of the previous section for the outward radiating ray (compare with Fig. 12). The analytic solution also implies that for larger wavenumber, larger shear, or smaller  $\beta$ , the tilt decreases faster when moving away from the jet core, which means that the ray is refracted more. Since it is the shear which is responsible for the refraction of the rays (through changing the meridional wavenumber  $l = l_0 \mp k_0 \Lambda t$ ), it is clear that a larger shear will cause larger refraction. The wavenumber depen-

dence is also clear, since larger wavenumbers corresponds to smaller waves, which are more easily influenced by the background shear. Finally,  $\beta$  has a competing effect with the shear.

### c. Comparison with numerical results

The validity of the analytic solution is now verified by comparing it with numerical ray tracing results. The ray equations (44) and (45) are solved using a basic forward Euler time-stepping. In Fig. 13 results of the ray tracing are plotted for different choices of initial zonal wavenumber,  $k_0$ . For the inward radiating ray, the ray is initiated just slightly below and above the upper and lower interfaces  $y = b, -b$  respectively.  $k_0$  is specified and  $l_0$  computed such that the eddy ellipse tilt (assuming plane wave solutions) is equal to the value diagnosed at that point from the simulation. That is, given  $k_0$  and  $y_0$ , we find  $l_0$  such that

$$\tan 2\theta(y_0) = \frac{2k_0 l_0}{k_0^2 - l_0^2}, \quad (49)$$

which gives two possible solutions for  $l_0$ . The sign is chosen such that the ray is directed towards the jet, i.e.,  $l_0 < 0$  in the northward side of the jet and  $l_0 > 0$  in the southward side of the jet. The possible values for  $k_0$  can be estimated using  $k^* \approx (\overline{v'v'}/\overline{\psi'\psi'})^{1/2}$ . This gives a typical value of  $k^* \approx 2.06 \times 10^{-5} \text{ m}^{-1}$  or, in normalized units,  $2k^*b \cong 3.1$  (where  $b = 75 \text{ km}$  is the width of the shear layer in each side of the jet). This is similar to the wavenumber that emerged in the simulation (mode  $n = 3$ , which corresponds to  $2kb \cong 3.24$ ).

In Fig. 13a the implied intrinsic group velocity from the ray tracing is plotted, for rays with varying zonal wavenumbers  $k_0 = 0.25k^*, 0.3k^*, 0.4k^*, 0.5k^*$  and  $0.9k^*$ , where the leftmost ray corresponds to the smallest wavenumber. The track for  $k_0 = 0.4k^*$  is highlighted in blue. In all cases, the initially southwestward pointing ray ends up pointing eastward, i.e.,  $\theta_{C_{gR}}$  tends towards zero as the rays approach the core of the jet, just as was found in the results from the numerical

simulation, analysed in section 3.2. The meridional component of the intrinsic group velocity, however, remains negative in the northward side of the jet, implying a positive eddy ellipse tilt, and vice-versa in the southward side of the jet, i.e. the momentum fluxes point out of the jet. Since the rays are plotted as a function of the zonal location  $x$  rather than time (as in Fig. 12), in Fig. 13b the time development of the highlighted ray with  $k_0 = 0.4k^*$  is plotted, in the same zonal location (the upper most arrow corresponds to  $t = 0$ , and the ray deflects as time progresses and it propagates towards the jet core). Note the remarkable similarity with Fig. 12 for the inward radiating ray during the unstable regime (albeit with a specific choice of  $k_0$ ).

For the outward radiating ray, the ray is initiated very close to the jet core ( $y = 0$ ) and hence  $l_0 = 0$  is chosen, which implies  $\theta = \pi/2$  and  $\theta_{c_{gR}} = 0$ . The sign of the ray tracing solution is chosen such that the ray is directed outwards from the jet, i.e.,  $l$  positive on the northward side of the jet and negative on the southward side of the jet. In Fig. 13c, the intrinsic group velocity from the ray tracing is plotted for the outward propagating rays for zonal wavenumbers  $k_0 = 0.2k^*, 0.26k^*, 0.3k^*, 0.34k^*$  and  $0.38k^*$  where the leftmost ray corresponds to the largest wavenumber. This is consistent with our earlier inspection of the analytic solution for the outward radiating ray, where it was found that larger wavenumbers will tend to be refracted more. The track for  $k_0 = 0.3k^*$  is highlighted in blue. In all cases,  $\theta_{c_{gR}}$  increases on the northward side and decreases in the southward side towards the jets flanks, similar to that observed in the simulation for the stable outward radiating regime. The meridional component of the intrinsic group velocity remains positive, which implies a negative eddy ellipse tilt in the northward side of the jet and vice-versa on the southward side of the jet, i.e., momentum fluxes into the jet. In Fig. 13d, the time development of the highlighted ray with  $k_0 = 0.3k^*$  is plotted, in the same zonal location. This is remarkably similar to Fig. 12 for the stable outward radiating regime (albeit, again, with a specific choice for  $k_0$ ).

Finally, in Fig. 14a,b the eddy ellipse tilts from the simulation and the ray tracing are compared, for the inward ( $t = 57$  days  $\approx 3\tau$ ) and outward ( $t = 155$  days  $\approx 8\tau$ ) radiating rays, respectively. This uses both the actual value for the tilt (black thick line), calculated from the simulation using the Reynolds stresses, as well as the estimated value (dashed thin red line) for a plane wave solution (19) using the estimated meridional and zonal wavenumbers  $l^* \approx (\overline{u'u'}/\overline{\psi'\psi'})^{1/2}$ ,  $k^* \approx (\overline{v'v'}/\overline{\psi'\psi'})^{1/2}$ , respectively, evaluated locally at every  $y$ . For the ray tracing solution,  $k_0 = 0.4k^*$  is chosen for the inward radiating ray and  $k_0 = 0.3k^*$  for the outward radiating ray (the blue rays in Figs. 13a and 13c, respectively). As a check for the analytic solution from the ray tracing equations, both the numerical (blue thin line) and the analytic solution (blue stars) are plotted for the eddy ellipse tilt, and these indeed coincide. The ray tracing agrees well with the simulation, albeit with the particular choices for the zonal wavenumbers as described above, and captures correctly the overall dependence of the tilt with  $y$ . These results validate the use of ray tracing predictions to predict eddy tilt.

## 5. Summary and discussion

In this manuscript, the role of eddy Reynolds stresses in accelerating and decelerating barotropic ocean jets has been revisited. In particular, the eddy Reynolds stresses have been analysed by exploring a geometric decomposition of the eddy stress tensor. This decomposition involves describing the eddy stress tensor in terms of an eddy variance ellipse, the geometry of which characterizes the mean eddy shape and orientation, the direction of eddy activity propagation, and the eddy forcing of the mean flow.

Idealized linear shear and jet profiles have been analysed and analytical results have been compared against fully nonlinear simulations. For flows with zero planetary vorticity gradient, analytic solutions have been obtained that provide a direct relationship between the geometric eddy tilt and

the phase difference of a normal mode solution. This allows a straightforward interpretation in terms of familiar concepts in classical stability theory. The initially unstable jet gives rise to eddies which are tilted “against the shear”; hence perturbations can grow and extract energy from the mean flow. However, as the jet becomes gradually weaker, at a given moment it can no longer satisfy the conditions for instability. Once the jet stabilizes, eddies become tilted “with the shear”, all perturbations decay as they return their energy to the mean flow and strengthen the jet. For cases with a non-zero planetary vorticity gradient, ray-tracing theory has been used to investigate eddy propagation within the jet, and make predictions for the evolution of the eddy wavenumber, which in turn can indicate the evolution of the eddy ellipse tilt. An analytic solution for the eddy tilt is found for the case of a linear plane Rossby wave propagating on a constant background shear. The ray tracing solution captures the essence of the observed eddy propagation and agrees well with the eddy tilt diagnosed from a fully nonlinear simulation, subject to a choice of initial zonal wavenumber.

We propose that the geometric framework explored in this manuscript could be used as a diagnostic tool to understand the role of Reynolds stresses in maintaining and decelerating inertial jets in ocean models and observations. For example, similar ideas have already been applied to separated western boundary currents such as the Gulf Stream and Kuroshio (Waterman and Hoskins 2013) and are currently being applied to the Southern Ocean to elucidate zonal jets embedded within the Antarctic Circumpolar Current (Klocker et al. 2016). For such problems, it would be interesting to apply the same ray tracing methods employed here to see if they can provide similar insights for flows that vary in a greater number of dimensions.

Moreover, we propose that the approach taken here might be employed to develop a simple parameterization of eddy Reynolds stresses for ocean general circulation models that are able to (at least partially) resolve inertial jets. While it is surely impractical to contemplate solving ray



equations in such models, one could imagine assuming that some of the eddy energy generated through baroclinic instability is back-scattered to the mean flow by up-gradient momentum transfer, as found in some of the idealized jet profiles in this manuscript, and proposed, for example, by Marshall and Adcroft (2010) and Jansen and Held (2014). The linear theory presented here suggests that the eddy tilt slightly deviates from that which might be expected from the argument that eddies should lean maximally with the mean shear, although the general picture of unstable eddies leaning (in the sense of eddy variance ellipse tilt) against the mean shear is observed. The anisotropy and eddy kinetic energy have in some cases been observed to counteract each others effects. In the zero beta cases the anisotropy and eddy kinetic energy both vary within the non-zero shear regions, but their product is constant. For the jet on a beta plane in the immediate jet core the eddy kinetic energy decreases with latitude, while the anisotropy increases.

The findings of this paper might be useful ingredients for a parameterization of horizontal eddy momentum fluxes. Exploiting the fact that the component of the eddy stress tensor involving the eddy Reynolds stresses is bounded by the eddy kinetic energy, assuming the momentum fluxes are directed either up-gradient or down-gradient, depending on the mean flow stability properties, and prescribing a typical value for the eddy anisotropy, it should be possible to develop a parameterization that is both energetically consistent and rooted in the underlying geometry of the eddy dynamics. However, even at the simplest level there remain many questions to be addressed. For example, should such a parameterization be applied to the depth-integrated flow? Furthermore it will be necessary to model the formation, propagation and dissipation of eddy kinetic energy, as discussed by Eden and Greatbatch (2008); Marshall and Adcroft (2010); Jansen et al. (2015). Despite these challenges, we believe this approach holds some promise and is worth exploring further.

## APPENDIX A

### Generalization of the relations for $M$ and $N$ between a pair of vorticity waves

The two isolated  $\delta$ -function vorticity waves can be generalized to the case where the vorticity field is continuous. Consider a zonal Fourier component of the vorticity anomaly,

$$q'(x, y, t) = \tilde{q}_k(y, t)e^{ikx} = \tilde{Q}_k(y, t)e^{i(kx + \varepsilon_k(y, t))}, \quad (\text{A1})$$

inducing a stream function anomaly of the form

$$\psi'(x, y, t) = \int \tilde{q}_k(x, y', t) G(y, y') dy' e^{ikx}, \quad (\text{A2})$$

where the Green's function is given by

$$G(y, y') = -\frac{1}{2k} e^{-k|y-y'|}. \quad (\text{A3})$$

After some algebra, we obtain

$$M = \iint \frac{\tilde{Q}_k(y', t) \tilde{Q}_k(y'', t)}{4} e^{-k(y' - y'')} \cos(\varepsilon_k(y'', t) - \varepsilon_k(y', t)) dy' dy'' \quad (\text{A4a})$$

$$N = - \iint \frac{\tilde{Q}_k(y', t) \tilde{Q}_k(y'', t)}{4} e^{-k(y' - y'')} \sin(\varepsilon_k(y'', t) - \varepsilon_k(y', t)) dy' dy'' \quad (\text{A4b})$$

Hence the values of  $M$  and  $N$  at some location  $y$  can be regarded as resulting from the continuum of infinite number of pairs of vorticity waves sandwiching  $y$  from below ( $y'$  contributions in the integral) and from above ( $y''$  contributions in the integral).

## APPENDIX B

### Numerical model description

For this study, we use PEQUOD (“Parallel Quasi-Geostrophic Model”), a finite difference code for solving quasi-geostrophic equations in a rectangular domain, configured in a one layer barotropic zonally periodic configuration. The numerical method implemented in PEQUOD and used here incorporates the Compact Accurately Boundary Adjusting high-Resolution Technique (CABARET) for advection of relative potential vorticity, combined with integration of the advection of planetary vorticity. Further details regarding CABARET can be found in Karabasov and Goloviznin (2007) and Karabasov et al. (2009). The potential vorticity inversion is performed using a fast Poisson solver using a customized version of FFTPACK.

The simulations are conducted in a rectangular domain  $-L \leq x \leq L$ ,  $-0.5L \leq y \leq 0.5L$  where  $L = 436$  km, with a no-slip boundary condition applied to the perturbation from the background profile, at all lateral boundaries. The model is integrated using a grid of  $n_x = 256$  and  $n_y = 129$  nodes in the zonal and meridional directions, respectively, corresponding to 3.4 km resolution and with a time step size of 52s. The model is then run for 287 days. The eddies are defined as deviations from the zonal mean, and the corresponding eddy quantities such as eddy kinetic energy, Reynolds stresses and the eddy variance ellipse parameters calculated accordingly.

The flow is initialised with the zonally symmetric jet  $U_0$ , and perturbed with small random noise. The numerical model essentially solves

$$\frac{Dq}{Dt} = \nu \nabla^2 q - r(q - q_{eq}) \quad (\text{B1})$$

where  $q = \nabla^2 \psi + \beta y$  is the absolute vorticity,  $\nu = 106 \text{ m}^2 \text{ s}^{-1}$  is a Laplacian viscosity coefficient parameter, and  $r = 5.2 \times 10^{-7} \text{ s}^{-1}$  is the relaxation time scale towards the background equilibrium flow  $q_{eq} = q_0$ . The jet strength is  $U_{0max} = 0.24 \text{ m s}^{-1}$ , and the jet half width is  $b = 75$  km. This corresponds to a shear of  $\Lambda = U_{0max}/b \cong 3.2 \times 10^{-6} \text{ s}^{-1}$ . For the case where the planetary vorticity gradient is nonzero, we use  $\beta = 2 \times 10^{-11} \text{ m}^{-1} \text{ s}^{-1}$  which corresponds to a non dimensional  $\beta$

(which measures the relative importance of the planetary vorticity gradient relative to the mean shear) of  $\beta^* = \beta b / \Lambda \cong 0.47$ . In midlatitudes, a typical ocean jet has  $U \sim 0.5 \text{ m s}^{-1}$  at the surface (e.g., Sheen et al. 2013), whereas the barotropic jet used here has a value more typical of the a depth-mean over the main thermocline.

## APPENDIX C

### Analytic solution for the ray tracing equations

Solving the ray equations (44) and (45) gives

$$k(t) = k_0, \quad l(t) = l_0 \pm k_0 \Lambda t, \quad (\text{C1})$$

where  $k_0, l_0$  are the initial wavenumbers.

Now using

$$\frac{dy}{dt} = \frac{2\beta k l}{(k^2 + l^2)^2} = \frac{2\beta}{k_0^2} \frac{\left(\frac{l_0}{k_0} \pm \Lambda t\right)}{\left[1 + \left(\frac{l_0}{k_0} \pm \Lambda t\right)^2\right]^2}, \quad (\text{C2})$$

gives

$$y(t) = y_c \mp \frac{\beta}{\Lambda k_0^2} \frac{1}{\left[1 + \left(\frac{l_0}{k_0} \pm \Lambda t\right)^2\right]} \quad (\text{C3})$$

where  $y_c$  is an integration constant. Similarly, using

$$\frac{dx}{dt} = \frac{\beta(k^2 - l^2)}{(k^2 + l^2)^2}, \quad (\text{C4})$$

gives

$$x(t) = x_c \mp \frac{\beta}{\Lambda k_0^2} \frac{\left(\frac{l_0}{k_0} \pm \Lambda t\right)}{\left[1 + \left(\frac{l_0}{k_0} \pm \Lambda t\right)^2\right]}. \quad (\text{C5})$$

These are the analytic solutions describing the ray path, following the intrinsic group velocity.

Now substituting (C1) in (19),

$$\cot \theta = -\frac{l_0}{k_0} \mp \Lambda t \quad (\text{C6})$$

681 and, substituting into (C3),

$$y(t) - y_c = \mp \frac{\beta}{\Lambda k_0^2} \sin^2 \theta = \mp \frac{\beta}{2\Lambda k_0^2} (1 - \cos 2\theta). \quad (C7)$$

682 At  $t = 0$ , we find:

$$y_0 - y_c = \pm \frac{\beta}{2\Lambda k_0^2} (1 - \cos 2\theta_0). \quad (C8)$$

683 Hence

$$y(\theta) = y_0 \pm \frac{\beta}{2\Lambda k_0^2} (\cos 2\theta - \cos 2\theta_0). \quad (C9)$$

684 Finally, solving for  $\theta$  gives

$$\theta(y) = \pm \frac{1}{2} \cos^{-1} \left( \cos 2\theta_0 \pm \frac{2\Lambda k_0^2}{\beta} (y - y_0) \right), \quad (C10)$$

685 which is (47), where  $\pm 2\Lambda k_0^2/\beta$  is positive in the northward side of the jet ( $y > 0$ ) and negative in  
 686 the southward side of the jet ( $y < 0$ ). The two possible  $\pm$  solutions corresponds to the two possible  
 687 solutions for  $l$ .

688 *Acknowledgments.* The authors would like to gratefully acknowledge useful discussions with  
 689 Laure Zanna and helpful comments by Julian Mak. The authors would also like to thank Stephanie  
 690 Waterman and Malte Jansen for comments that significantly improved the article. TT acknowl-  
 691 edges support by the Israeli Science Foundation through a grant to Yohai Kaspi (ISF 1310/12).  
 692 JRM and DPM acknowledge the support of the Natural Environment Research Council grant num-  
 693 ber NE/L005166/1. The numerical code used in this article was developed from an original code  
 694 provided by Pavel S. Berloff (see also Karabasov et al. 2009).

## 695 References

696 Bretherton, F. P., 1966a: Baroclinic instability, the short wave cutoff in terms of potential vorticity.  
 697 *Q. J. R. Meteorol. Soc.*, **92**, 335–345.

698 Bretherton, F. P., 1966b: Critical layer instability in baroclinic flows. *Quarterly Journal of the*  
699 *Royal Meteorological Society*, **92 (393)**, 325–334.

700 Buhler, O., 2009: *Waves and Mean Flows*. Cambridge University Press, 341 pp.

701 Danabasoglu, G., J. C. McWilliams, and P. R. Gent, 1994: The role of mesoscale tracer transport  
702 in the global ocean circulation. *Science*, **264**, 1123–1126.

703 Davies, H. C., and C. H. Bishop, 1994: Eady edge waves and rapid development. *J. Atmos. Sci.*,  
704 **51**, 1930–1946.

705 Eden, C., 2010: Parameterising meso-scale eddy momentum fluxes based on potential vorticity  
706 mixing and a gauge term. *Ocean Modelling*, **32 (1-2)**, 58–71.

707 Eden, C., and R. J. Greatbatch, 2008: Towards a mesoscale eddy closure. *Ocean Modelling*, **20 (3)**,  
708 223–239.

709 Fox Kemper, B., R. Lumpkin, and F. Bryan, 2013: Lateral transport in the ocean. *Ocean Cir-*  
710 *culation and Climate (Second edition)*, G. Siedler, J. Church, J. Gould, and S. Griffies, Eds.,  
711 185–209.

712 Gent, P. R., and J. C. McWilliams, 1990: Isopycnal mixing in ocean circulation models. *Journal*  
713 *of Physical Oceanography*, **20 (1)**, 150–155.

714 Gent, P. R., J. Willebrand, T. J. McDougall, and J. C. McWilliams, 1995: Parameterizing eddy-  
715 induced tracer transports in ocean circulation models. *Journal of Physical Oceanography*,  
716 **25 (4)**, 463–474.

717 Greatbatch, R. J., 1998: Exploring the relationship between eddy-induced transport velocity, ver-  
718 tical momentum transfer, and the isopycnal flux of potential vorticity. *J. Phys. Oceanogr.*, **28**,  
719 422–432.

720 Heifetz, E., C. H. Bishop, B. J. Hoskins, and P. Alpert, 1999: Counter-propagating Rossby waves  
 721 in barotropic Rayleigh model of shear instability. *Q. J. R. Meteorol. Soc.*, **125**, 2835–2853.

722 Heifetz, E., and J. Methven, 2005: Relating optimal growth to counterpropagating Rossby waves  
 723 in shear instability. *Phys. Fluids*, **17** (6), 064 107, doi:10.1063/1.1937064, URL <http://scitation.aip.org/content/aip/journal/pof2/17/6/10.1063/1.1937064>.  
 724

725 Hoskins, B. J., and T. Ambrizzi, 1993: Rossby wave propagation on a realistic longitudinally  
 726 varying flow. *J. Atmos. Sci.*, **50**, 1661–1671.

727 Hoskins, B. J., I. N. James, and G. H. White, 1983: The shape, propagation and mean-flow inter-  
 728 action of large-scale weather systems. *Journal of the Atmospheric Sciences*, **40** (7), 1595–1612.

729 Hoskins, B. J., and D. J. Karoly, 1981: The steady linear response of a spherical atmosphere to  
 730 thermal and orographic forcing. *J. Atmos. Sci.*, **38**, 1179–1196.

731 Hoskins, B. J., M. E. McIntyre, and A. W. Robertson, 1985: On the use and significance of  
 732 isentropic potential vorticity maps. *Q. J. R. Meteorol. Soc.*, **111**, 877.

733 Huang, H.-P., A. Kaplan, E. N. Curchitser, and N. A. Maximenko, 2007: The degree of anisotropy  
 734 for mid-ocean currents from satellite observations and an eddy-permitting model simulation.  
 735 *Journal of Geophysical Research: Oceans*, **112** (C9), c09005.

736 Jansen, M., A. Adcroft, R. Hallberg, and I. Held, 2015: Parameterization of eddy fluxes based on  
 737 a mesoscale energy budget. *Ocean Modell.*, doi:10.1016/j.ocemod.2015.05.007.

738 Jansen, M., and I. Held, 2014: Parameterizing subgrid-scale eddy effects using energetically con-  
 739 sistent backscatter. *Ocean Modell.*, **80**, 36–48.

740 Johnson, G. C., and H. L. Bryden, 1989: On the size of the Antarctic Circumpolar Current. *Deep*  
 741 *Sea Res.*, **36**, 39–53.

742 Karabasov, A., P. Berloff, and V. Goloviznin, 2009: CABARET in the ocean gyre. *Ocean Model-*  
743 *ing*, **30**, 155–168.

744 Karabasov, A., and V. Goloviznin, 2007: A new efficient high-resolution method for non-linear  
745 problems in fluid mechanics. *New Trends in Fluid Mechanics Research*, Springer, **1**, 269–272.

746 Klocker, A., J. R. Maddison, D. P. Marshall, and A. C. Naveira Garabato, 2016: Wave-turbulence-  
747 mean flow interaction in the Antarctic Circumpolar Current. *Under review in Journal of Physical*  
748 *Oceanography*.

749 Lighthill, J., 1977: *Waves in Fluids*. Cambridge University Press, 504 pp.

750 Maddison, J. R., and D. P. Marshall, 2013: The Eliassen-Palm flux tensor. *Journal of Fluid Me-*  
751 *chanics*, **729**, 69–102.

752 Maddison, J. R., D. P. Marshall, and J. Shipton, 2015: On the dynamical influence of ocean eddy  
753 potential vorticity fluxes. *Ocean Modelling*, **92**, 169–182.

754 Marshall, D. P., and A. J. Adcroft, 2010: Parameterization of ocean eddies: Potential vorticity  
755 mixing, energetics and Arnold’s first stability theorem. *Ocean Modelling*, **32 (3-4)**, 188–204.

756 Marshall, D. P., J. R. Maddison, and P. S. Berloff, 2012: A framework for parameterizing eddy  
757 potential vorticity fluxes. *Journal of Physical Oceanography*, **42 (4)**, 539–557.

758 Morrow, R., R. Coleman, J. Church, and D. Chelton, 1994: Surface eddy momentum flux and  
759 velocity variances in the Southern Ocean from Geosat altimetry. *Journal of Physical Oceanog-*  
760 *raphy*, **24 (10)**, 2050–2071.

761 Pedlosky, J., 1987: *Geophysical fluid dynamics*. 2nd ed., Springer-Verlag.



762 Plumb, R. A., 1986: Three-dimensional propagation of transient quasi-geostrophic eddies and its  
763 relationship with the eddy forcing of the time-mean flow. *Journal of the Atmospheric Sciences*,  
764 **43 (16)**, 1657–1678.

765 Preisendorfer, R. W., 1988: *Principal component analysis in meteorology and oceanography*,  
766 Developments in Atmospheric Science, Vol. 17. Elsevier.

767 Rayleigh, L., 1880: On the stability, or instability, of certain fluid motions. *proc. London Math.*  
768 *Soc.*, **9**, 57–70.

769 Rossby, C., 1939: Relation between variation in the intensity of the zonal circulation of the atmo-  
770 sphere and the displacement of the semi-permanent centers of action. *J. Mar. Res.*, **2**, 38–55.

771 Salmon, R., 1998: *Lectures on geophysical fluid dynamics*. Oxford University Press.

772 Scott, R. B., B. K. Arbic, C. L. Holland, A. Sen, and B. Qiu, 2008: Zonal versus meridional  
773 velocity variance in satellite observations and realistic and idealized ocean circulation models.  
774 *Ocean Modelling*, **23 (3-4)**, 102–112.

775 Sheen, K. L., and Coauthors, 2013: Rates and mechanisms of turbulent dissipation and mixing  
776 in the Southern Ocean: Results from the Diapycnal and Isopycnal Mixing Experiment in the  
777 Southern Ocean (DIMES). *J. Geophys. Res. Ocean.*, **118**, 2774–2792.

778 Stewart, K. D., P. Spence, S. Waterman, J. Le Sommer, J.-M. Molines, J. M. Lilly, and M. H.  
779 England, 2015: Anisotropy of eddy variability in the global ocean. *Ocean Modelling*, **95**, 53–  
780 65.

781 Taylor, G. I., 1915: Eddy motion in the atmosphere. *Philosophical Transactions for the Royal*  
782 *Society of London. Series A, Containing Papers of a Mathematical or Physical Character*, **215**,  
783 1–26.

- 784 Waterman, S., N. G. Hogg, and S. R. Jayne, 2011: Eddy-mean flow interaction in the Kuroshio  
785 Extension region. *Journal of Physical Oceanography*, **41** (6), 1182–1208.
- 786 Waterman, S., and B. J. Hoskins, 2013: Eddy shape, orientation, propagation, and mean flow  
787 feedback in western boundary current jets. *Journal of Physical Oceanography*, **43** (8), 1666–  
788 1690.
- 789 Waterman, S., and S. Jayne, 2012: Eddy-driven recirculations from a localized, transient forcing.  
790 *J. Phys. Oceanogr.*, **42**, 430–447.
- 791 Waterman, S., and S. R. Jayne, 2011: Eddy-mean flow interactions in the along-stream develop-  
792 ment of a western boundary current jet: An idealized model study. *Journal of Physical Oceanog-*  
793 *raphy*, **41** (4), 682–707.
- 794 Waterman, S., and J. M. Lilly, 2015: Geometric decomposition of eddy feedbacks in barotropic  
795 systems. *Journal of Physical Oceanography*, **45** (4), 1009–1024.
- 796 Whitham, G., 1974: *Linear and Nonlinear Waves*. New York: Wiley-Interscience.
- 797 Wilkin, J. L., and R. A. Morrow, 1994: Eddy kinetic energy and momentum flux in the Southern  
798 Ocean: Comparison of a global eddy-resolving model with altimeter, drifter, and current-meter  
799 data. *Journal of Geophysical Research: Oceans*, **99** (C4), 7903–7916.

## LIST OF FIGURES

- Fig. 1.** Illustration of the geometric properties of the eddy variance ellipse: the magnitude, tilt, and eccentricity. A: Two ellipses with equal tilt and eccentricity and differing magnitude, corresponding to locally higher (solid line) and lower (dashed line) eddy kinetic energy. B: Two ellipses with equal magnitude and eccentricity and differing tilt, corresponding to the case where the  $x$ -component of the eddy velocity results in the greatest eddy momentum stress (solid line) and where the component at 45 degrees to the  $x$ -axis results in the greatest eddy momentum stress (dashed line). C: Two ellipses with equal magnitude and tilt and differing eccentricity, corresponding to higher (solid line) and lower (dashed line) eddy momentum stress magnitude resulting from the component of the eddy velocity in the minor axis direction. . . . . 46
- Fig. 2.** a)  $u'-v'$  space ellipse which captures the geometric structure of the local eddy covariance tensor, with semi-major axis  $A$ , semi-minor axis  $B$ , and focus separation  $2F$  (see also Marshall et al. (2012) Fig. 3 (a) and Waterman and Lilly (2015) Fig. 1). b) Tilt angle  $\theta$  octants, and the corresponding signs of the eddy Reynolds stresses  $M$  and  $N$  (see also Waterman and Hoskins 2013, figure 2). . . . . 47
- Fig. 3.** Illustration of geometric parameter patterns which, subject to zonal averaging, lead to an eastward momentum tendency. In each case exactly one of  $K$ ,  $\gamma$ , or  $\theta$  varies with  $y$ . A:  $K$  decreasing with  $y$ , with  $0 < \theta < \pi/2$ . B:  $K$  increasing with  $y$ , with  $-\pi/2 < \theta < 0$ . C:  $\gamma$  decreasing with  $y$ , with  $0 < \theta < \pi/2$ . D:  $\gamma$  increasing with  $y$ , with  $-\pi/2 < \theta < 0$ . E:  $\theta$  decreasing with  $y$ , with  $-\pi/4 < \theta < \pi/4$ . F:  $\theta$  increasing with  $y$ , with  $-\pi/2 < \theta < -\pi/4$  or  $\pi/4 < \theta \leq \pi/2$ . . . . . 48
- Fig. 4.** Illustration of geometric parameter patterns which, subject to zonal averaging, lead to a westward momentum tendency. In each case exactly one of  $K$ ,  $\gamma$ , or  $\theta$  varies with  $y$ . A:  $K$  increasing with  $y$ , with  $0 < \theta < \pi/2$ . B:  $K$  decreasing with  $y$ , with  $-\pi/2 < \theta < 0$ . C:  $\gamma$  increasing with  $y$ , with  $0 < \theta < \pi/2$ . D:  $\gamma$  decreasing with  $y$ , with  $-\pi/2 < \theta < 0$ . E:  $\theta$  increasing with  $y$ , with  $-\pi/4 < \theta < \pi/4$ . F:  $\theta$  decreasing with  $y$ , with  $-\pi/2 < \theta < -\pi/4$  or  $\pi/4 < \theta \leq \pi/2$ . . . . . 49
- Fig. 5.** Schematic illustration of two isolated vorticity waves and their induced velocities, when the waves are (a) in phase ( $\epsilon_k = 0$ ), and (b)  $\pi/2$  out of phase ( $\epsilon_k = \pi/2$ ). The  $\pm q$  represent the vorticity anomalies, the circular arrows show the circulation they induce, and the thick arrows represent their associated velocities. The red and dashed blue arrows represent the induced velocities from the upper and lower waves, respectively. The figure illustrates how  $|M|$  ( $|N|$ ) is maximized when the waves are in phase ( $\pi/2$  out of phase). . . . . 50
- Fig. 6.** Normalised eddy kinetic energy  $K/Q_k^2$  and anisotropy  $\gamma$  for the most unstable mode for the Rayleigh profile (with equal amplitude waves at  $y = \pm b$ ). The background velocity profile is shown on the left. Corresponding eddy ellipses are shown on the right, with the foci of the ellipses indicated by red filled circles. . . . . 51
- Fig. 7.** (a) The piecewise linear jet model of two shear layer with constant vorticity of opposite signs embedded by two infinite layers of zero vorticity. At  $y = 0, \pm 1$  the mean flow vorticity is discontinuous, and supports the existence of three waves on each of the interfaces. (b) Snapshot of relative vorticity ( $s^{-1}$ ) at some initial time evolution, after  $t = 57$  days, shows the most unstable normal mode configuration of three phase locked waves which are tilted against the shear. (c) The eddy ellipse tilt given by the theoretical normal mode solution for the infinite domain (blue line) is constant within each side of the jet, and equals  $\theta \cong \pm 0.2\pi$ . This is in good agreement with the snapshot from a numerical simulation (red dashed line)

at  $t = 57$  days. (d) The eddy ellipse anisotropy from the analytic solution (blue) and the numerical simulation (dashed red). At  $y = 0$  and near the interfaces at  $y = \pm 1$  the anisotropy maximizes. Here  $y$  and  $x$  are the meridional and zonal coordinates, respectively, normalized by  $b$ . . . . . 52

**Fig. 8.** (a) Zonal mean velocity (normalized by  $U_{0max} = 0.24 \text{ m s}^{-1}$ ) at three different times of the evolution of the nonzero beta case. The initial piecewise linear jet ( $t = 0$  days, black solid line) weakens and broadens significantly due to eddies fluxing momentum out of the jet ( $t = 135$  days  $\approx 7\tau$ , red), but later strengthens due to upgradient fluxes ( $t = 172$  days  $\approx 9\tau$ , dashed blue). (b) Zonal mean potential vorticity (normalized by  $\Lambda = 3.2 \times 10^{-6} \text{ s}^{-1}$ ) and (c) mean potential vorticity gradient (normalized by  $b^{-1}\Lambda = 4.2 \times 10^{-11} \text{ m}^{-1} \text{ s}^{-1}$ ), for three different times of the evolution. Time is in units of days, where  $\tau = 19$  days and  $y$  is the meridional coordinate normalized by  $b$ . . . . . 53

**Fig. 9.** Snapshots of the potential vorticity for the non zero beta jet ( $\text{s}^{-1}$ ) at different times of the evolution (time units is given in days). (a)  $t = 57$  days  $\approx 3\tau$ , the most unstable mode is apparent and the interfaces are characterized by a wavy structure. (b)  $t = 115$  days  $\approx 6\tau$ , the system is no longer in the linear stage as the waves merged into vortices, however they are still clearly tilted against the shear. (c)  $t = 155$  days  $\approx 8\tau$ , the tilt flips and the vortices are now tilted with the shear. (d)  $t = 270$  days  $\approx 14\tau$ , the vortices break and the system equilibrates. Time is in units of days ( $\tau = 19$  days) and coordinates ( $x, y$ ) are normalized by  $b$ . . . . . 54

**Fig. 10.** Scatter plots of  $(u', v')$  at different times and meridional locations ( $\text{m s}^{-1}$ ): at the initial linear stage,  $t = 57$  days  $\approx 3\tau$  (left column), at some intermediate time,  $t = 115$  days  $\approx 6\tau$ , before the eddy tilt had flipped (middle column) and at  $t = 155$  days  $\approx 8\tau$  after the eddy tilt had flipped (right column). This is shown for meridional locations of  $y = b$  (upper row),  $y = 0$  (middle row) and  $y = -b$  (lower row). The red ellipse in each panel shows the corresponding ellipse. Time is in units of days, where  $\tau = 19$  days. . . . . 55

**Fig. 11.** Temporal evolution and meridional structure of (a) eddy ellipse tilt (normalized by  $\pi$ ), (b) anisotropy, (c)  $N$  ( $\text{m}^2 \text{s}^{-2}$ ), (d)  $M$  ( $\text{m}^2 \text{s}^{-2}$ ), (e)  $\log(K/K_0)$  (where  $K_0 = 1 \text{ m}^2 \text{s}^{-2}$ ), and (f)  $\log(L/L_0)$  (where  $L = \gamma K$  and  $L_0 = 1 \text{ m}^2 \text{s}^{-2}$ ). Note that the colorbar is cyclic in (a), and that log scale with base 10 is used in (e) and (f). Time is given in units of  $\tau = 19$  days, and  $y$  is the meridional coordinate normalized by  $b$ . . . . . 56

**Fig. 12.** Direction of the implied intrinsic (relative) group velocity  $\theta_{c_{gR}}$ . Arrows show  $(\cos \theta_{c_{gR}}, \sin \theta_{c_{gR}})$  and therefore denote only the direction of propagation. Time is given in units of  $\tau = 19$  days (where  $\tau$  is the inverse growth rate of the fastest growing wavenumber on the  $f$ -plane), and  $y$  is the meridional coordinate normalized by  $b$ . . . . . 57

**Fig. 13.** (a) Direction of intrinsic group velocity from ray tracing results for the inward radiating ray, for varying zonal wavenumbers:  $k_0 = 0.25k^*, 0.3k^*, 0.4k^*, 0.5k^*, 0.9k^*$ . The leftmost ray corresponds to the smallest wavenumber. The track for  $k_0 = 0.4k^*$  is highlighted in blue. (b) The time evolution of the highlighted ray with  $k_0 = 0.4k^*$ , in the same zonal location. (c) Outward radiating ray, for varying zonal wavenumbers:  $k_0 = 0.2k^*, 0.26k^*, 0.3k^*, 0.34k^*, 0.38k^*$ . The leftmost ray corresponds to the largest wavenumber. The track for  $k_0 = 0.3k^*$  is highlighted in blue. (d) The time evolution of the highlighted ray with  $k_0 = 0.3k^*$ , in the same zonal location. Note that in all panels arrows are unitless and show only the direction of intrinsic group velocity, at zonal locations that propagate with the full group velocity. Here  $y$  and  $x$  are the meridional and zonal coordinates, respectively, normalized by  $b$ . . . . . 58

891 **Fig. 14.** Eddy ellipse tilt (normalized by  $\pi$ ), for (a) inward radiating ray ( $t = 57$  days  $\approx 3\tau$ ) and (b)  
 892 outward radiating ray ( $t = 155$  days  $\approx 8\tau$ ). Compared are actual tilt from the simulation  
 893 calculated directly from the Reynolds stresses (black), estimated value using the planewave  
 894 assumption with estimated wavenumbers  $k^*, l^*$  from the simulation (dashes red), ray tracing  
 895 results from numerical (light blue) and analytic (blue stars) solutions. See text for explana-  
 896 tion. Here  $y$  is the meridional coordinate normalized by  $b$ . . . . . 59

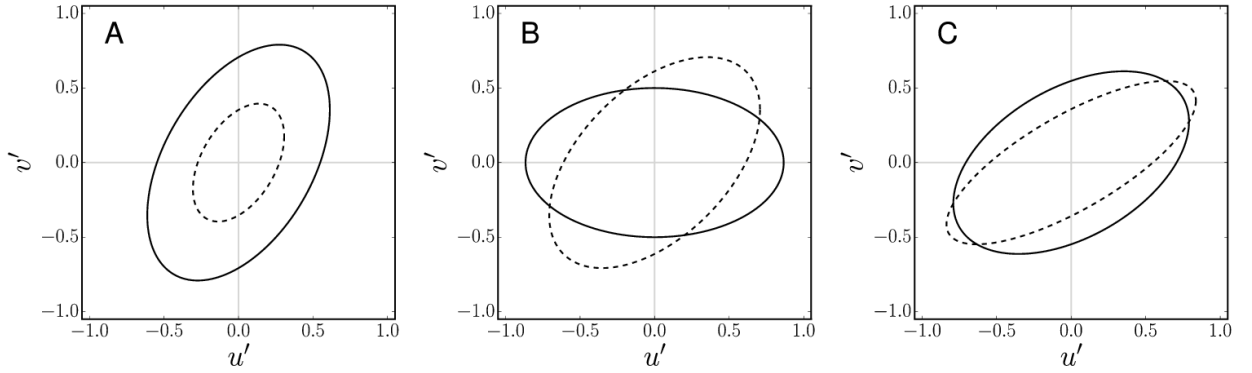
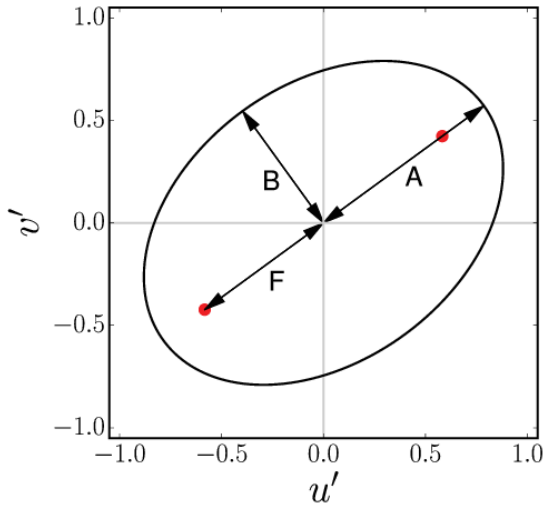


FIG. 1. Illustration of the geometric properties of the eddy variance ellipse: the magnitude, tilt, and eccentricity. A: Two ellipses with equal tilt and eccentricity and differing magnitude, corresponding to locally higher (solid line) and lower (dashed line) eddy kinetic energy. B: Two ellipses with equal magnitude and eccentricity and differing tilt, corresponding to the case where the  $x$ -component of the eddy velocity results in the greatest eddy momentum stress (solid line) and where the component at 45 degrees to the  $x$ -axis results in the greatest eddy momentum stress (dashed line). C: Two ellipses with equal magnitude and tilt and differing eccentricity, corresponding to higher (solid line) and lower (dashed line) eddy momentum stress magnitude resulting from the component of the eddy velocity in the minor axis direction.

**a**



**b**

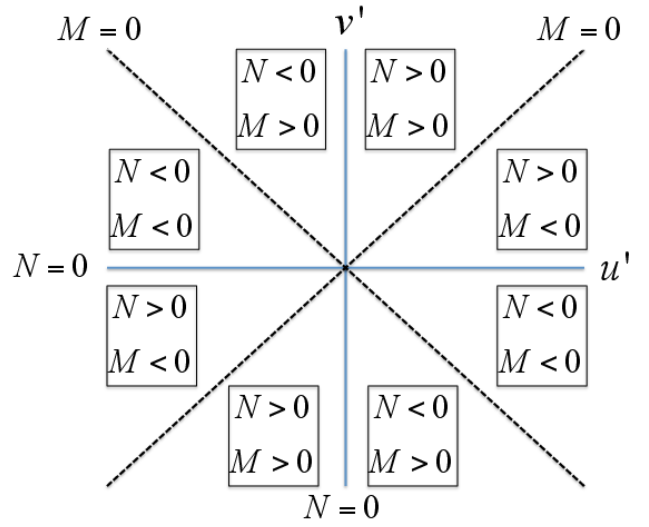
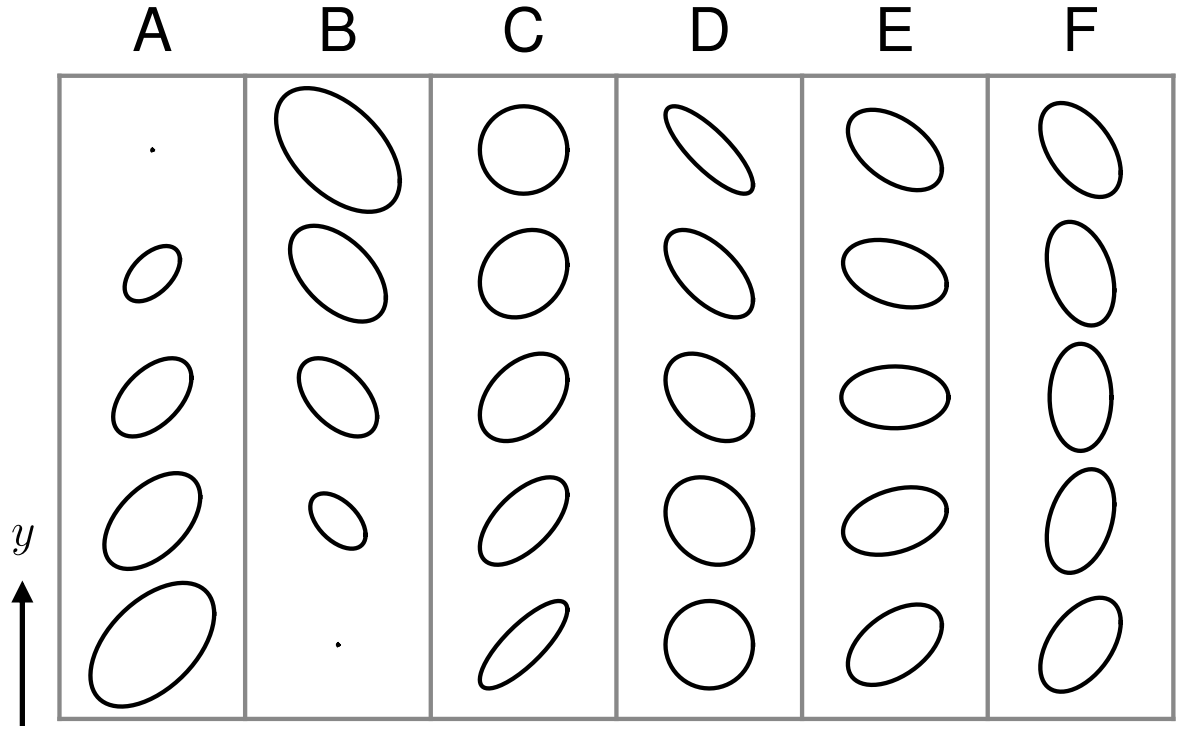
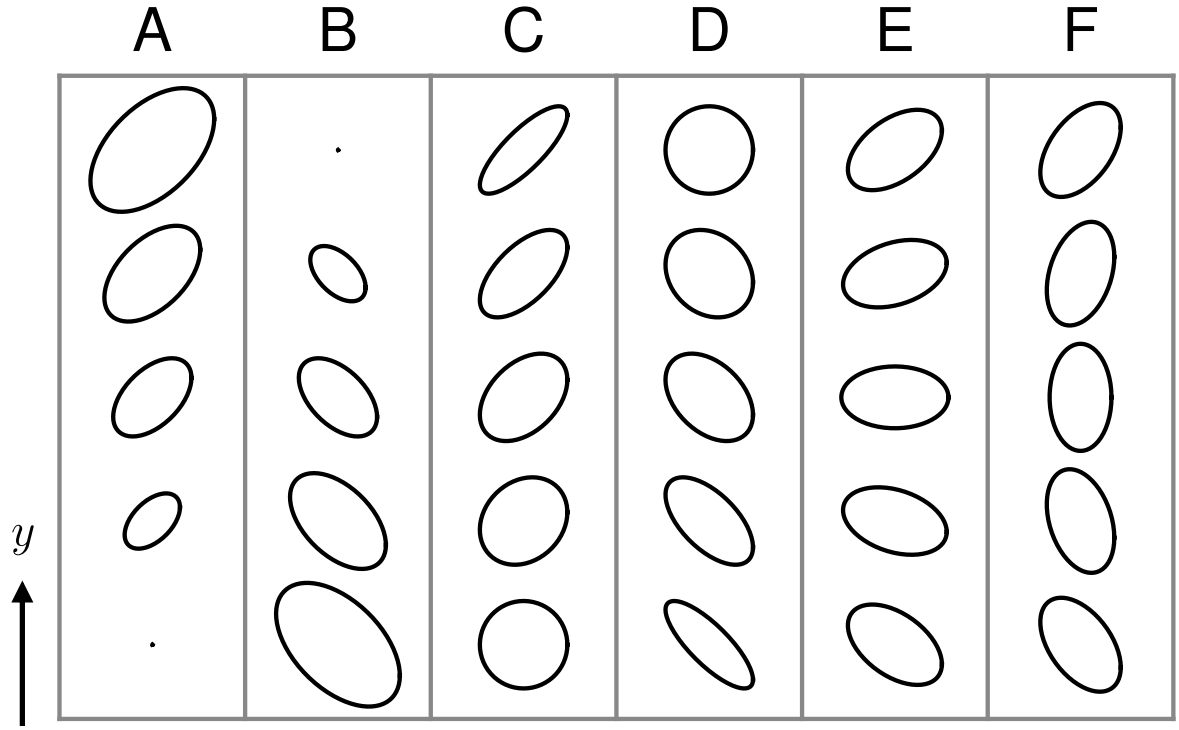


FIG. 2. a)  $u'$ - $v'$  space ellipse which captures the geometric structure of the local eddy covariance tensor, with semi-major axis  $A$ , semi-minor axis  $B$ , and focus separation  $2F$  (see also Marshall et al. (2012) Fig. 3 (a) and Waterman and Lilly (2015) Fig. 1). b) Tilt angle  $\theta$  octants, and the corresponding signs of the eddy Reynolds stresses  $M$  and  $N$  (see also Waterman and Hoskins 2013, figure 2).



909 FIG. 3. Illustration of geometric parameter patterns which, subject to zonal averaging, lead to an eastward  
 910 momentum tendency. In each case exactly one of  $K$ ,  $\gamma$ , or  $\theta$  varies with  $y$ . A:  $K$  decreasing with  $y$ , with  
 911  $0 < \theta < \pi/2$ . B:  $K$  increasing with  $y$ , with  $-\pi/2 < \theta < 0$ . C:  $\gamma$  decreasing with  $y$ , with  $0 < \theta < \pi/2$ . D:  $\gamma$   
 912 increasing with  $y$ , with  $-\pi/2 < \theta < 0$ . E:  $\theta$  decreasing with  $y$ , with  $-\pi/4 < \theta < \pi/4$ . F:  $\theta$  increasing with  $y$ ,  
 913 with  $-\pi/2 < \theta < -\pi/4$  or  $\pi/4 < \theta \leq \pi/2$ .





914 FIG. 4. Illustration of geometric parameter patterns which, subject to zonal averaging, lead to a westward  
 915 momentum tendency. In each case exactly one of  $K$ ,  $\gamma$ , or  $\theta$  varies with  $y$ . A:  $K$  increasing with  $y$ , with  
 916  $0 < \theta < \pi/2$ . B:  $K$  decreasing with  $y$ , with  $-\pi/2 < \theta < 0$ . C:  $\gamma$  increasing with  $y$ , with  $0 < \theta < \pi/2$ . D:  $\gamma$   
 917 decreasing with  $y$ , with  $-\pi/2 < \theta < 0$ . E:  $\theta$  increasing with  $y$ , with  $-\pi/4 < \theta < \pi/4$ . F:  $\theta$  decreasing with  $y$ ,  
 918 with  $-\pi/2 < \theta < -\pi/4$  or  $\pi/4 < \theta \leq \pi/2$ .

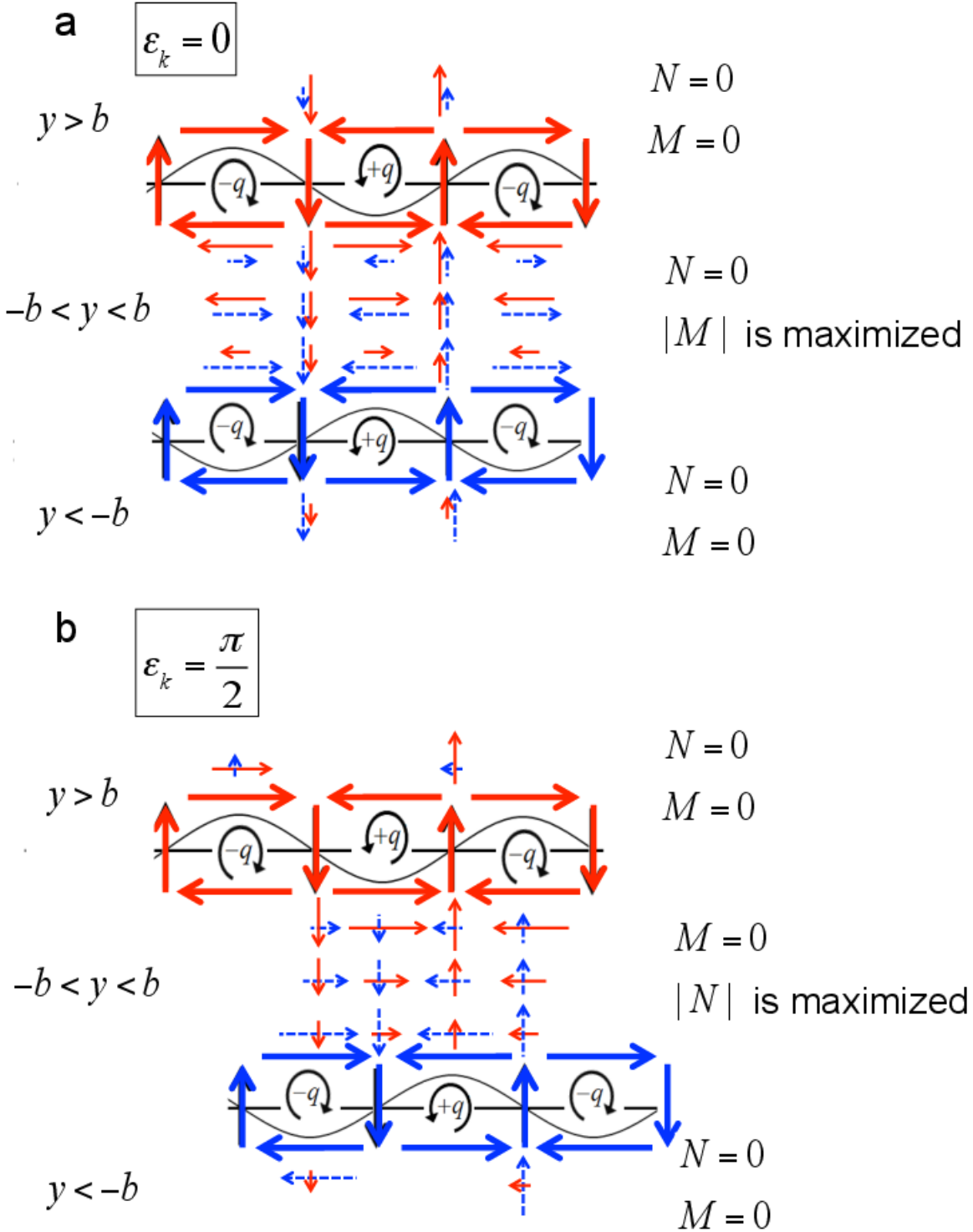


FIG. 5. Schematic illustration of two isolated vorticity waves and their induced velocities, when the waves are (a) in phase ( $\epsilon_k = 0$ ), and (b)  $\pi/2$  out of phase ( $\epsilon_k = \pi/2$ ). The  $\pm q$  represent the vorticity anomalies, the circular arrows show the circulation they induce, and the thick arrows represent their associated velocities. The red and dashed blue arrows represent the induced velocities from the upper and lower waves, respectively. The figure illustrates how  $|M|$  ( $|N|$ ) is maximized when the waves are in phase ( $\pi/2$  out of phase).

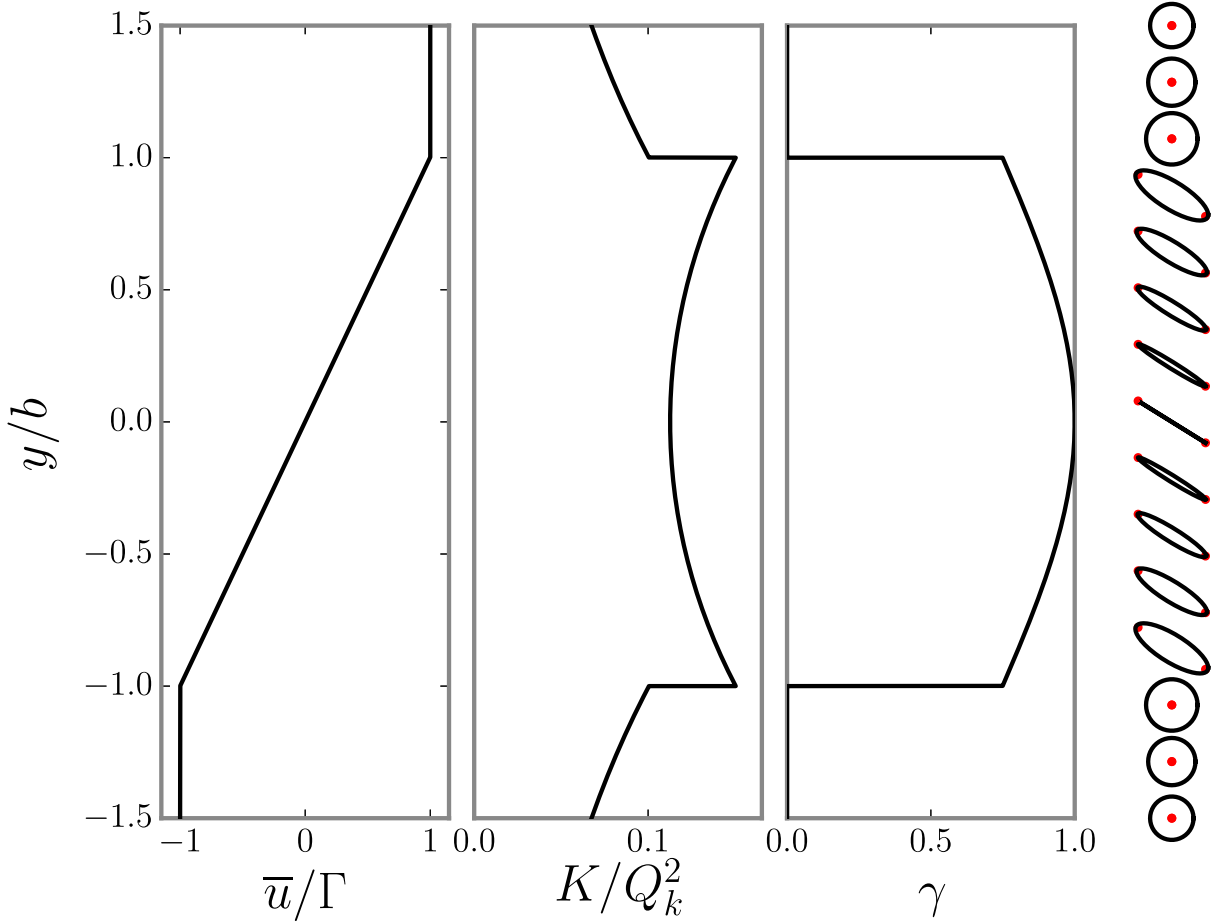


FIG. 6. Normalised eddy kinetic energy  $K/Q_k^2$  and anisotropy  $\gamma$  for the most unstable mode for the Rayleigh profile (with equal amplitude waves at  $y = \pm b$ ). The background velocity profile is shown on the left. Corresponding eddy ellipses are shown on the right, with the foci of the ellipses indicated by red filled circles.

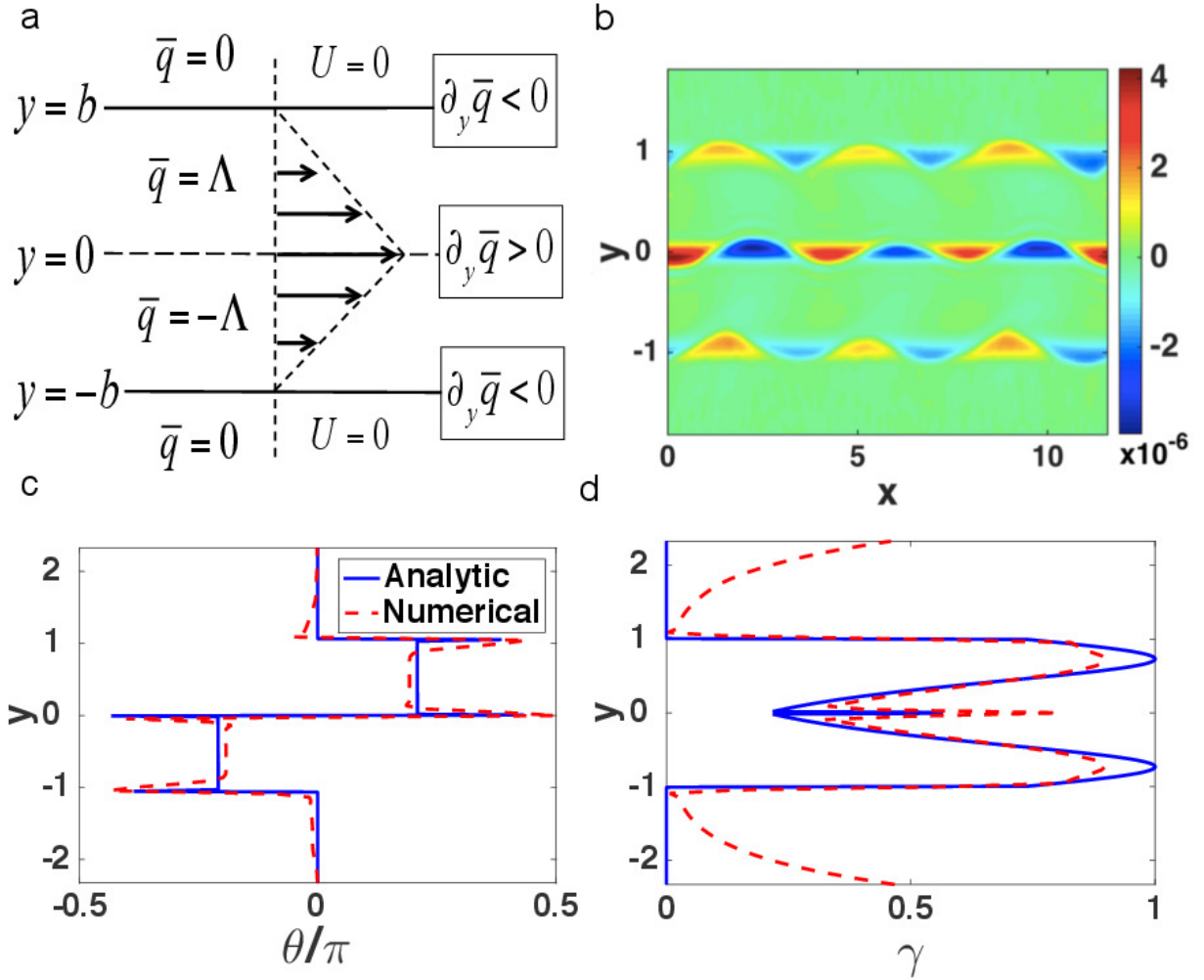


FIG. 7. (a) The piecewise linear jet model of two shear layer with constant vorticity of opposite signs embedded by two infinite layers of zero vorticity. At  $y = 0, \pm 1$  the mean flow vorticity is discontinuous, and supports the existence of three waves on each of the interfaces. (b) Snapshot of relative vorticity ( $s^{-1}$ ) at some initial time evolution, after  $t = 57$  days, shows the most unstable normal mode configuration of three phase locked waves which are tilted against the shear. (c) The eddy ellipse tilt given by the theoretical normal mode solution for the infinite domain (blue line) is constant within each side of the jet, and equals  $\theta \cong \pm 0.2\pi$ . This is in good agreement with the snapshot from a numerical simulation (red dashed line) at  $t = 57$  days. (d) The eddy ellipse anisotropy from the analytic solution (blue) and the numerical simulation (dashed red). At  $y = 0$  and near the interfaces at  $y = \pm 1$  the anisotropy maximizes. Here  $y$  and  $x$  are the meridional and zonal coordinates, respectively, normalized by  $b$ .

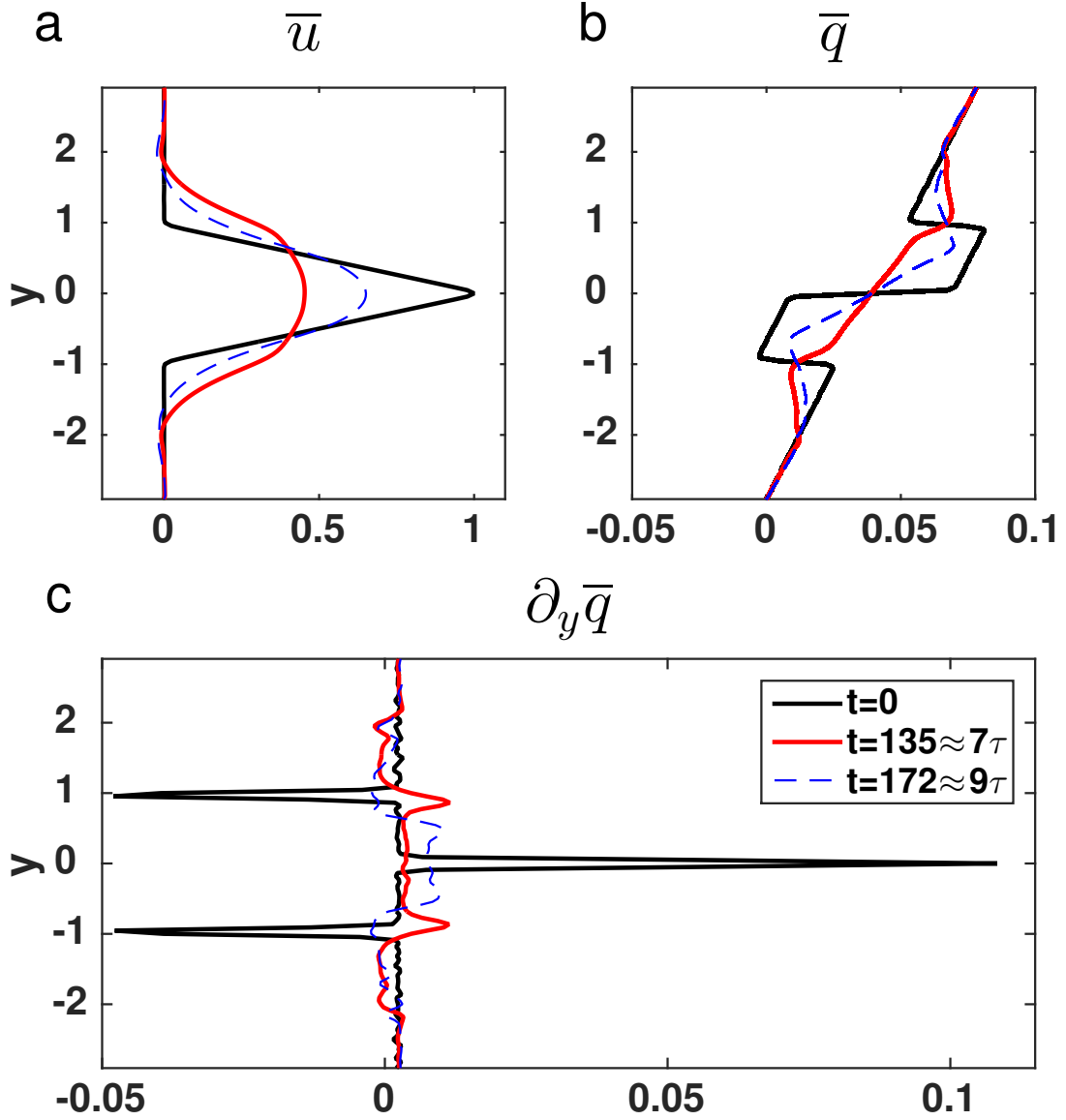
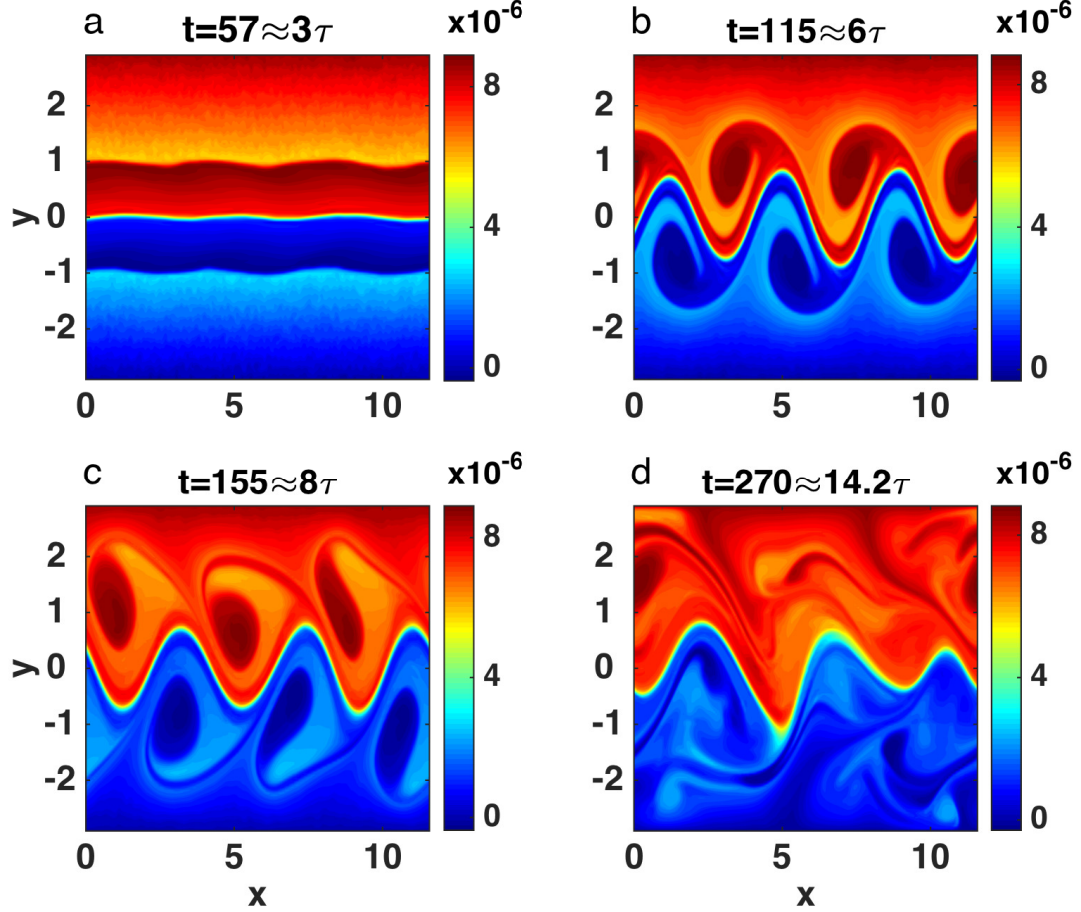
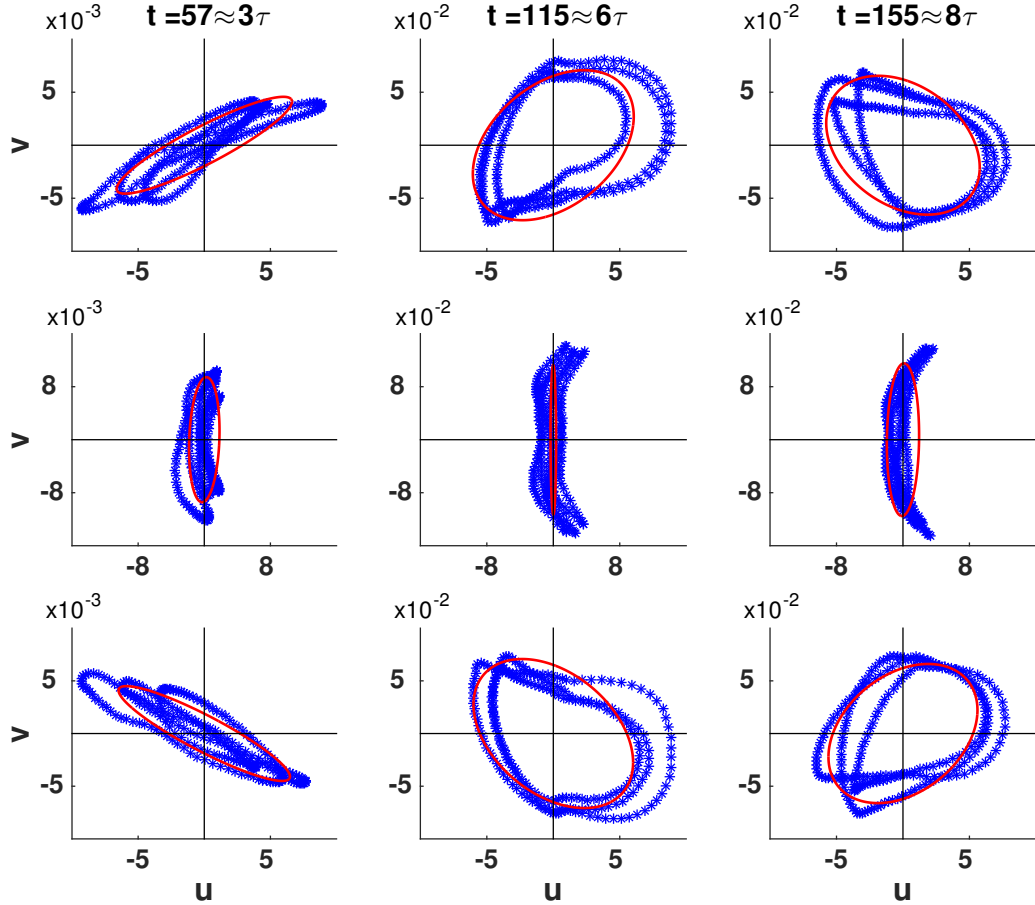


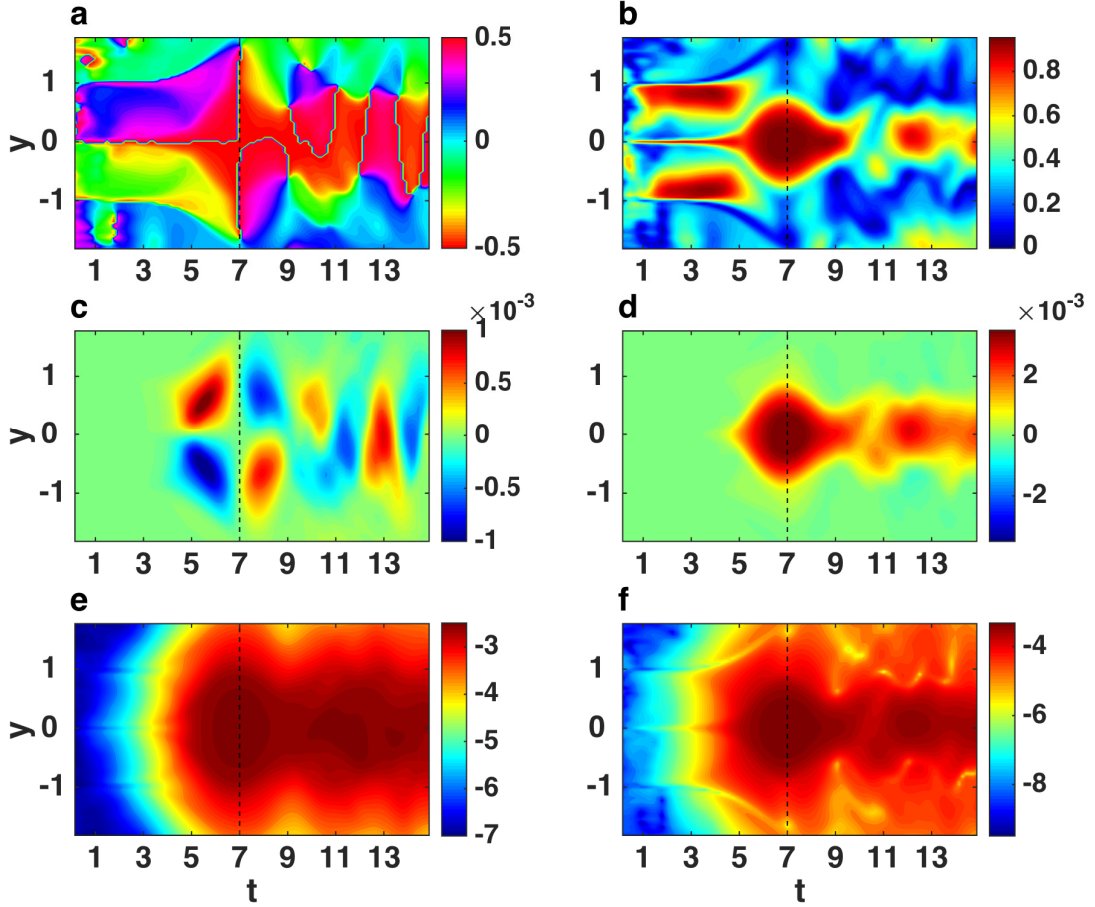
FIG. 8. (a) Zonal mean velocity (normalized by  $U_{0max} = 0.24 \text{ ms}^{-1}$ ) at three different times of the evolution of the nonzero beta case. The initial piecewise linear jet ( $t = 0$  days, black solid line) weakens and broadens significantly due to eddies fluxing momentum out of the jet ( $t = 135$  days  $\approx 7\tau$ , red), but later strengthens due to upgradient fluxes ( $t = 172$  days  $\approx 9\tau$ , dashed blue). (b) Zonal mean potential vorticity (normalized by  $\Lambda = 3.2 \times 10^{-6} \text{ s}^{-1}$ ) and (c) mean potential vorticity gradient (normalized by  $b^{-1} \Lambda = 4.2 \times 10^{-11} \text{ m}^{-1} \text{ s}^{-1}$ ), for three different times of the evolution. Time is in units of days, where  $\tau = 19$  days and  $y$  is the meridional coordinate normalized by  $b$ .



944 FIG. 9. Snapshots of the potential vorticity for the non zero beta jet ( $s^{-1}$ ) at different times of the evolution  
 945 (time units is given in days). (a)  $t = 57$  days  $\approx 3\tau$ , the most unstable mode is apparent and the interfaces are  
 946 characterized by a wavy structure. (b)  $t = 115$  days  $\approx 6\tau$ , the system is no longer in the linear stage as the waves  
 947 merged into vortices, however they are still clearly tilted against the shear. (c)  $t = 155$  days  $\approx 8\tau$ , the tilt flips and  
 948 the vortices are now tilted with the shear. (d)  $t = 270$  days  $\approx 14\tau$ , the vortices break and the system equilibrates.  
 949 Time is in units of days ( $\tau = 19$  days) and coordinates  $(x,y)$  are normalized by  $b$ .

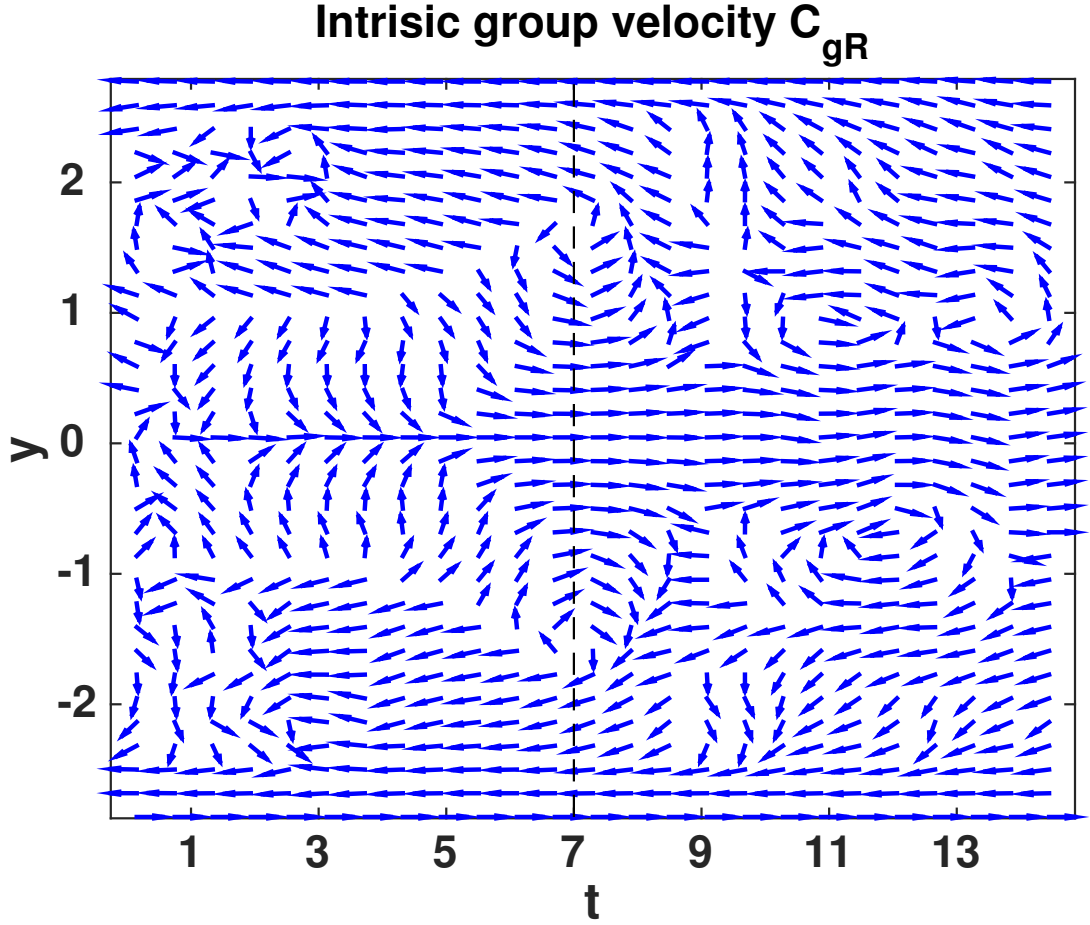


950 FIG. 10. Scatter plots of  $(u', v')$  at different times and meridional locations ( $\text{ms}^{-1}$ ): at the initial linear stage,  
 951  $t = 57 \text{ days} \approx 3\tau$  (left column), at some intermediate time,  $t = 115 \text{ days} \approx 6\tau$ , before the eddy tilt had flipped  
 952 (middle column) and at  $t = 155 \text{ days} \approx 8\tau$  after the eddy tilt had flipped (right column). This is shown for  
 953 meridional locations of  $y = b$  (upper row),  $y = 0$  (middle row) and  $y = -b$  (lower row). The red ellipse in each  
 954 panel shows the corresponding ellipse. Time is in units of days, where  $\tau = 19 \text{ days}$ .



955 FIG. 11. Temporal evolution and meridional structure of (a) eddy ellipse tilt (normalized by  $\pi$ ), (b) anisotropy,  
 956 (c)  $N$  ( $\text{m}^2\text{s}^{-2}$ ), (d)  $M$  ( $\text{m}^2\text{s}^{-2}$ ), (e)  $\log(K/K_0)$  (where  $K_0 = 1 \text{ m}^2\text{s}^{-2}$ ), and (f)  $\log(L/L_0)$  (where  $L = \gamma K$  and  
 957  $L_0 = 1 \text{ m}^2\text{s}^{-2}$ ). Note that the colorbar is cyclic in (a), and that log scale with base 10 is used in (e) and (f). Time  
 958 is given in units of  $\tau = 19$  days, and  $y$  is the meridional coordinate normalized by  $b$ .





959 FIG. 12. Direction of the implied intrinsic (relative) group velocity  $\theta_{c_{gR}}$ . Arrows show  $(\cos \theta_{c_{gR}}, \sin \theta_{c_{gR}})$   
 960 and therefore denote only the direction of propagation. Time is given in units of  $\tau = 19$  days (where  $\tau$  is  
 961 the inverse growth rate of the fastest growing wavenumber on the f-plane), and  $y$  is the meridional coordinate  
 962 normalized by  $b$

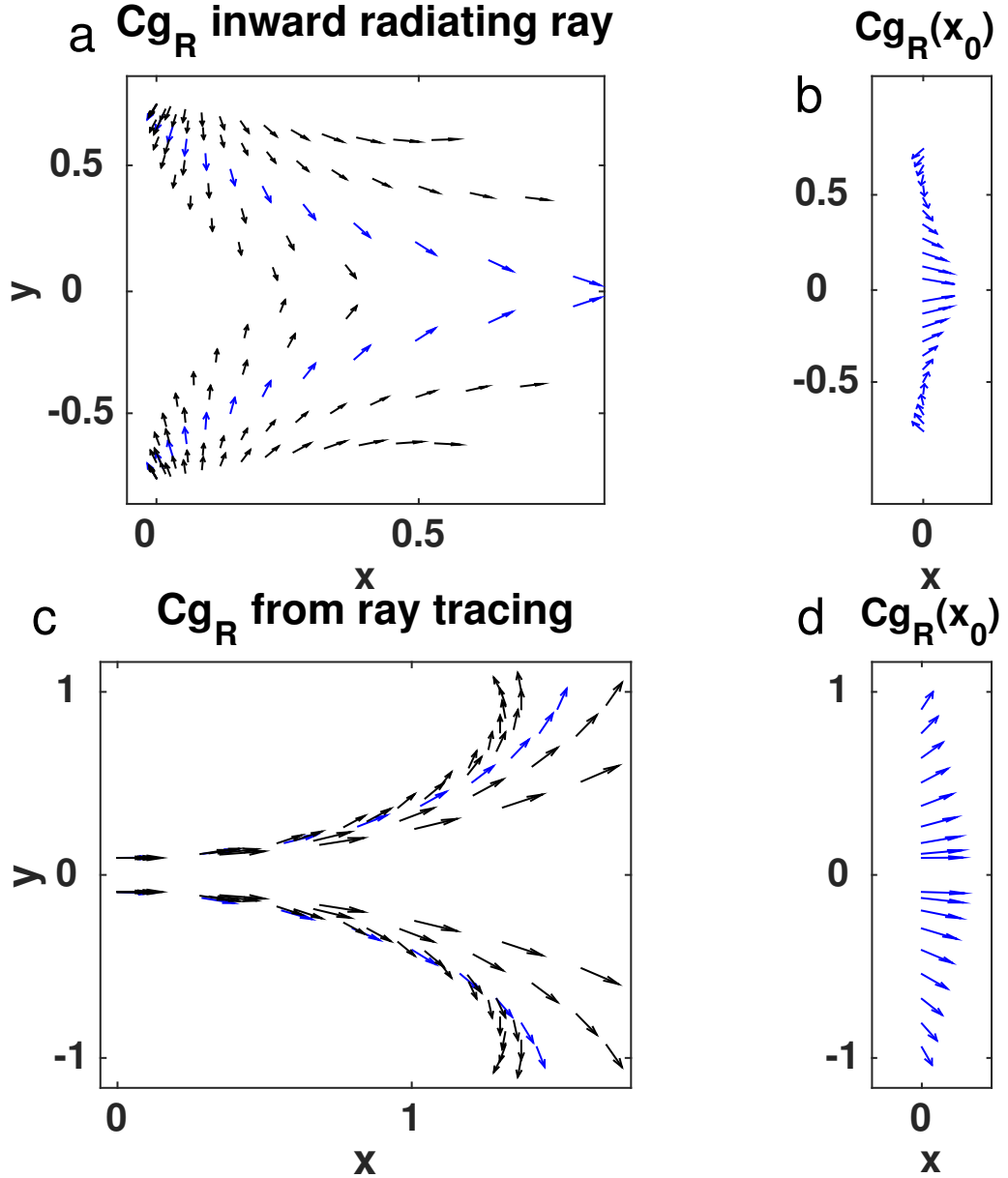


FIG. 13. (a) Direction of intrinsic group velocity from ray tracing results for the inward radiating ray, for varying zonal wavenumbers:  $k_0 = 0.25k^*, 0.3k^*, 0.4k^*, 0.5k^*, 0.9k^*$ . The leftmost ray corresponds to the smallest wavenumber. The track for  $k_0 = 0.4k^*$  is highlighted in blue. (b) The time evolution of the highlighted ray with  $k_0 = 0.4k^*$ , in the same zonal location. (c) Outward radiating ray, for varying zonal wavenumbers:  $k_0 = 0.2k^*, 0.26k^*, 0.3k^*, 0.34k^*, 0.38k^*$ . The leftmost ray corresponds to the largest wavenumber. The track for  $k_0 = 0.3k^*$  is highlighted in blue. (d) The time evolution of the highlighted ray with  $k_0 = 0.3k^*$ , in the same zonal location. Note that in all panels arrows are unitless and show only the direction of intrinsic group velocity, at zonal locations that propagate with the full group velocity. Here  $y$  and  $x$  are the meridional and zonal coordinates, respectively, normalized by  $b$ .

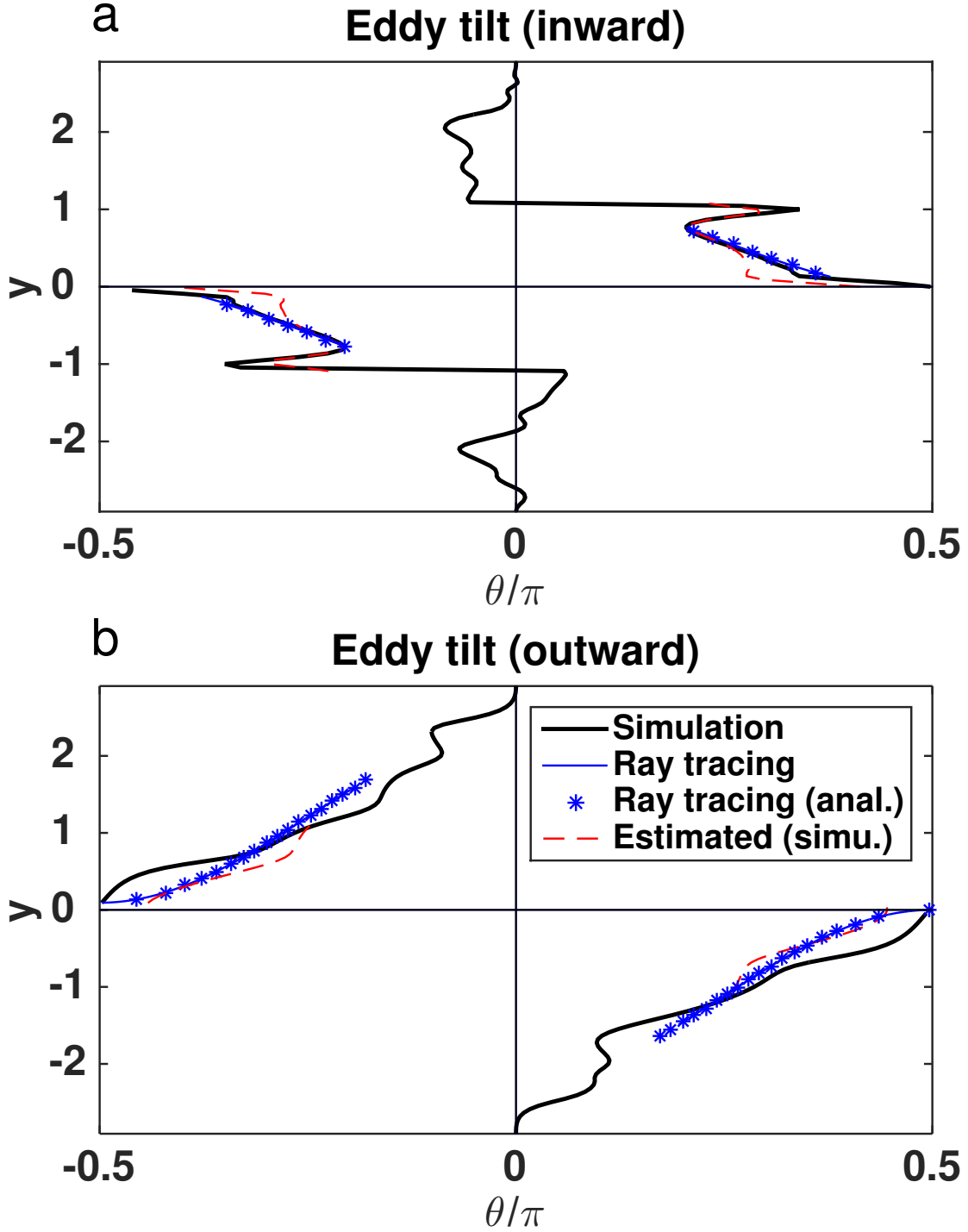


FIG. 14. Eddy ellipse tilt (normalized by  $\pi$ ), for (a) inward radiating ray ( $t = 57$  days  $\approx 3\tau$ ) and (b) outward radiating ray ( $t = 155$  days  $\approx 8\tau$ ). Compared are actual tilt from the simulation calculated directly from the Reynolds stresses (black), estimated value using the planewave assumption with estimated wavenumbers  $k^*, l^*$  from the simulation (dashes red), ray tracing results from numerical (light blue) and analytic (blue stars) solutions. See text for explanation. Here  $y$  is the meridional coordinate normalized by  $b$ .